POLITECNICO
MILANO 1863

SCUOLA DI INGEGNERIA INDUSTRIALE
E DELL'INFORMAZIONE

von KARMAN INSTITUTE
FOR FLUID DYNAMICS

Iterative model-based approach for the estimation of integral length scales from experimental data

Tesi di Laurea Magistrale in
Mechanical Engineering - Ingegneria Meccanica

Author: **Chiara Casilli**

Student ID: 11016223
Advisor: Prof. Paolo Gaetani
Co-advisor: Prof. Fabrizio Fontaneto
Academic Year: 2025-2026

Abstract

Accurate characterization of inflow turbulence, including intensity, time and length scales, is necessary to understand loss mechanisms and heat transfer in turbomachinery flows. Such characterization is also essential for the calibration and validation of CFD models, which are widely used in the design and optimization of turbomachinery but remain limited in capturing complex aerodynamic phenomena.

Among turbulence descriptors, the integral length scale (Λ) represents the size of the largest energy-containing motions in a turbulent flow and is one of the main parameters that characterize free-stream turbulence. Together with turbulence intensity, it can affect the boundary-layer state, promoting transition and potentially inducing separation. However, its experimental estimation remains challenging, as measurement noise and methodological choices can lead to significant variability between tests.

This study focuses on estimating integral length scales from experimental data acquired from SPLEEN C1 low-pressure turbine cascade tested in the low speed wind tunnel at the von Kármán Institute. Several conventional methods, based on autocorrelation and spectral analysis, are evaluated, highlighting their sensitivity to case-dependent parameters and uncertainties in integration limits or frequency ranges. To overcome these limitations, alternative iterative approaches based on the von Kármán spectrum and Pope's model are developed. These methods demonstrate improved robustness and consistency for sufficiently long signals, reducing sensitivity to subjective choices and providing more reliable estimates of Λ.

Keywords: integral length scale, spectral analysis, autocorrelation, turbulence characterization, low pressure turbine

Abstract in lingua italiana

Una caratterizzazione accurata della turbolenza in ingresso, inclusi intensità, scale temporali e scale spaziali, è fondamentale per comprendere i meccanismi di perdita e di trasferimento di calore nei flussi di turbomacchine. Tale caratterizzazione è inoltre essenziale per la calibrazione e la validazione dei modelli CFD (Computational Fluid Dynamics), ampiamente impiegati nella progettazione e nell'ottimizzazione delle turbomacchine, ma ancora limitati nella capacità di descrivere fenomeni aerodinamici complessi. Tra i descrittori della turbolenza, la scala integrale (Λ) rappresenta la dimensione dei vortici più grandi e maggiormente energetici ed è uno dei parametri principali che caratterizzano la turbolenza del flusso indisturbato (free-stream). Insieme all'intensità di turbolenza, Λ può influenzare in modo significativo lo stato dello strato limite, promuovendo la transizione e potenzialmente inducendo fenomeni di separazione. Tuttavia, la sua stima sperimentale rimane complessa: il rumore della misura, la lunghezza finita dei segnali acquisiti e le scelte metodologiche possono introdurre una marcata variabilità tra diverse prove sperimentali, compromettendo la riproducibilità e l'affidabilità delle stime.

Il presente studio si concentra sulla stima delle scale integrali della turbolenza a partire da dati sperimentali acquisiti su una schiera di pale di turbina di bassa pressione SPLEEN C1, testata nella galleria del vento a bassa velocità del von Kármán Institute for Fluid Dynamics (VKI). Diversi metodi convenzionali, basati sulla funzione di autocorrelazione e sull'analisi spettrale, sono stati analizzati, mettendone in evidenza i limiti e le principali fonti di incertezza, tra cui la sensibilità alla scelta dei limiti di integrazione e degli intervalli di frequenza considerati. Per superare tali limitazioni, è stato sviluppato e implementato un approccio iterativo fondato sullo spettro di von Kármán e sul modello di Pope. Questo metodo mostra maggiore robustezza e affidabilità per segnali sufficientemente lunghi, riducendo la dipendenza da scelte soggettive e fornendo stime più consistenti e accurate della scala integrale della turbolenza Λ.

Parole chiave: scala integrale della turbolenza, analisi spettrale, autocorrelazione, caratterizzazione della turbolenza, turbina di bassa pressione

Contents

Nomenclature

α	flow yaw angle, temperature coefficient of resistance
α_1	inlet geometrical angle
α_2	outlet geometrical angle
β	flow pitch angle, empirical constant controlling dissipative range decay
$\boldsymbol{\kappa}$	wavenumber vector
δ	wedge angle
$\dot{m}_h$	injected mass flow rate from the active grid
$\dot{m}$	mass flow rate in the test section
ℓ	generic eddy size
ℓ_0	largest eddy scale
ℓ_{DI}	length scale separating inertial and dissipation ranges
ℓ_{EI}	length scale separating energy-containing and inertial ranges
η	Kolmogorov microscale, temperature recovery factor
Γ	gamma function ([26]Eq. 3.67)
γ	stagger angle, air specific heat ratio
$\hat{\mathbf{u}}$	Fourier coefficient
κ	wavenumber magnitude
κ_1	streamwise wavenumber
κ_e	wavenumber of largest eddy
Λ	integral length scale

Λ_x	streamwise component of the integral length scale
$\langle\cdot\rangle$	ensemble average, time average under statistical stationarity (Eq. 2.2)
$\mathbf{u}$	fluid velocity vector
$\mathbf{u}'$	fluctuating velocity vector
$\mathbf{x}$	position
$\mathcal{L}$	mean flow length scale
$\mathcal{T}$	integral time scale
Tu	turbulence intensity
μ	dynamic viscosity
ν	kinematic viscosity
Φ_{ij}	velocity spectrum tensor (Eq. 2.15)
ρ	density
$\rho(\tau)$	autocorrelation coefficient
τ	time lag
$\tau*$	time lag of first zero-crossing
ε	turbulent kinetic energy dissipation rate
ε_{ss}	rear suction side turning angle
a	overheat ratio
C, C_1, C_2	constants of the 3D and 1D inertial subrange model
C_h	chord
c_L, c_η	empirical constants in Pope's spectrum model
C_{ax}	axial chord
d	grid bars diameter
$E(\kappa)$	three-dimensional energy spectrum
E_b	Bridge voltage
E_{11}	streamwise one-dimensional energy spectrum

f	frequency
f_η	Non-dimensional function describing the shape of the dissipation range
f_L	Non-dimensional function describing the shape of the energy-containing range spectrum
F_s	sampling frequency
f_{max}	upper limit of the frequency range used for spectrum fitting or averaging
f_{min}	lower limit of the frequency range used for spectrum fitting or averaging
g	pitch
k	turbulent kinetic energy, thermal conductivity
l	active wire length
M	Mach number
m	moment order(Eq. 2.2)
Nu	Nusselt number
o	cascade throat
P	static pressure
P_0	total pressure
p_0	slope of 3D energy spectrum at low wavenumbers
R	specific gas constant for dry air
R_t	Wheatstone bridge top resistance
R_w	wire resistance
R_ℓ	lead resistance
R_{ij}	two-point velocity correlation or spatial correlation
R_{le}	leading edge curvature radius
R_{ref}	wire resistance at ambient temperature
R_{te}	trailing edge curvature radius
R_{tot}	total resistance of the hot wire electrical circuit
R_{uu}	autocorrelation function

Re	Reynolds number
Re_w	wire Reynolds number
$Re_{2,is}$	cascade outlet isentropic Reynolds number
Re_{eff}	Effective Reynolds number sensed by the wire
$S(\kappa)$	spherical shell of radius κ in wavenumber space
T	static temperature, signal duration
t	time
T_0	total temperature
T_{adw}	recovery temperature
t_{maz}	maximum blade thickness
T_{ref}	ambient temperature
U	mean flow velocity
u'	streamwise fluctuating component of velocity, equal to u'_1
u'_i	fluctuating velocity component
u_{rms}	velocity root mean square
v'	transversal fluctuating component of velocity, equal to u'_2
x_1	streamwise direction

1| Introduction

The development and design of modern turbomachinery rely heavily on computational fluid dynamics (CFD) as a primary tool for aerodynamic performance prediction and optimization. Due to computational time and cost constraints, these simulations are often performed using low-fidelity approaches, which, despite their efficiency, struggle to accurately capture complex flow phenomena.

As discussed by Denton [11], the accuracy of CFD predictions is affected by several sources of uncertainty, including numerical discretization, boundary conditions, and physical modeling assumptions. Among these, the representation of turbulence and laminar-to-turbulent transition remains a major source of error, leading to significant inaccuracies in loss prediction and flow separation behavior. In particular, RANS solvers are highly sensitive to the choice of transition and turbulence models and often fail to reproduce the detailed physics of boundary layer development and wake formation [29].

These limitations are especially critical in low-pressure turbines (LPTs), where cruise operating conditions promote laminar–turbulent transition and flow separation on the blade suction side. Both phenomena strongly influence profile losses, which constitute the dominant contribution to the overall loss budget in LPT stages.

Free-stream turbulence intensity and length scales strongly influence the boundary-layer state, including transition onset, separation bubbles, and turbulent reattachment, and therefore the associated momentum loss mechanisms [20].

To overcome the intrinsic limitations of RANS modeling, high-fidelity approaches such as Large Eddy Simulation (LES) and Direct Numerical Simulation (DNS) provide a more detailed representation of turbulent structures. However, these methods require the generation of realistic turbulent inflow conditions and their validation against reliable experimental data. In turbomachinery applications the accurate reproduction of free-stream turbulence is therefore essential for trustworthy numerical predictions.

The reliability of both low- and high-fidelity simulations ultimately depends on the quality of the experimental data used for validation. Yet turbulence quantities are inherently difficult to measure with high precision. They are affected by significant experimen-

tal uncertainty and often rely on strong assumptions during signal processing [5]. This challenge is particularly complicated for turbulence length scales, which typically exhibit larger uncertainty than turbulence intensity.

In this context the von Karman Institute (VKI) is conducting an experimental campaign in a low-speed turbine cascade rig equipped with turbulence generators capable of producing a wide range of free-stream turbulence conditions. The campaign aims to systematically characterize turbulence by varying intensity and length scales, allowing these two key parameters to be decoupled and studied independently. The tests are performed on a low-speed scaled version of the SPLEEN C1 cascade, a transonic LPT geometry representative of modern geared turbofan architectures previously tested by VKI.

A central objective of this thesis is the development of a robust methodology for processing integral length scales from grid turbulence experimental data. Conventional approaches, i.e. autocorrelation function and power spectrum based methods, are affected by different sources of uncertainty, such as test-to-test variability or inaccurate estimation of the spectrum at the low-frequencies. An alternative iterative methodology is proposed to overcome these limitations, providing a more reliable estimation of turbulence length scales for future research.

1.1. Thesis outline

This thesis is organized into six chapters, progressively guiding the reader from the theoretical foundations of turbulence to the development and validation of the proposed methodology for integral length scale estimation.

Chapter 1 introduces the research context and motivations. The importance of accurately characterizing free-stream turbulence for turbomachinery applications is discussed, with particular emphasis on the challenges associated with the estimation of turbulence length scales from experimental data. The objectives and scope of the present work are also defined.

Chapter 2 presents the theoretical background necessary for the development of the proposed methodology. Fundamental concepts of turbulence are reviewed, including the energy cascade mechanism and Kolmogorov's similarity hypotheses. The spectral representation of turbulence is then discussed, and classical energy spectrum models, including the von Kármán and Pope formulations, are presented as the theoretical basis for the subsequent analysis.

Chapter 3 describes the experimental setup employed in the present study. The VKI C-1

low-speed wind tunnel and the low-speed SPLEEN C1 cascade are introduced, together with the turbulence grids used to generate controlled free-stream turbulence conditions. The measurement systems, including hot-wire anemometry instrumentation and data acquisition procedures, are also discussed.

Chapter 4 introduces the proposed iterative model-based approach for integral length scale estimation. The limitations of classical autocorrelation- and spectrum-based definitions are first analyzed. The conceptual framework of the new method is then presented, including the definition of the objective function, the spectral fitting strategy, and the numerical minimization procedure. An uncertainty analysis is performed to evaluate three main sources of uncertainty, namely methodological, statistical, and measurement-related contributions.

Chapter 5 presents the experimental results obtained by applying the proposed methodology to different turbulence configurations. The method is first validated on a reference test case, including a repeatability assessment. Its robustness is then evaluated across different grid configurations, operating conditions, and active grid injection modes.

Finally, **Chapter 6** summarizes the main findings of the study, highlights the contributions of the proposed methodology, and outlines possible directions for future research and implementation.

2| Theoretical background

This chapter presents the theoretical background required for turbulence characterization and length-scale estimation methods developed in this work. The discussion begins with a qualitative description of turbulence and its defining physical features, followed by an overview of the energy cascade mechanism that governs the transfer of kinetic energy across scales. The cascade is then interpreted from a spectral perspective, introducing the energy spectrum as a key tool for visualizing and quantifying the distribution of turbulent energy in wavenumber space. The chapter concludes with the presentation of energy spectrum models that form the basis of the integral length-scale estimation methods adopted in this thesis.

2.1. Turbulence

Turbulence is a fundamental phenomenon in fluid mechanics that occurs in most natural and engineering flows, significantly enhancing the transport of momentum, heat, and mass while also contributing to fluid friction losses and flow-induced noise. It is characterized as a three-dimensional, unsteady, and rotational motion with fluctuations of flow quantities in both time and space.

The physical origin of turbulence lies in the intrinsic non-linearity of the governing Navier–Stokes equations, particularly in the convective term. The role of this non-linearity is quantified by Reynolds number $\mathrm{Re} = U\mathcal{L}/\nu$, whose value drastically influences the character of the flow regime. As the Reynolds number increases beyond a problem-dependent critical value, the initially ordered laminar flow becomes unstable: fluid-dynamic instabilities disrupt regular velocity profiles, leading to the formation of unsteady vortical structures. These structures undergo further instabilities, rapidly cascading into a chaotic flow state that is theoretically impossible to predict in detail, thus necessitating turbulence modeling.

The progression from laminar to turbulent flow, known as transition, occurs as a result of a limited succession of instabilities, which at a certain point evolve into fully turbulent

flow, which resembles deterministic chaos.
Kundu, Cohen and Dowling [17] describe turbulent flows with five generic qualities:

(1) *Fluctuations:* flow quantities exhibit chaotic fluctuations even in presence of time-invariant boundary conditions

(2) *Nonlinearity:* turbulence is caused by the non-linear nature of the governing equations, and it occurs when the relevant nonlinearity parameter, such as Re, exceeds a critical value.

(3) *Vorticity:* Turbulence appears as a mix of streaks, strain regions, and swirls of varying sizes that deform and interact. Spinning structures are called eddies, which exist over a range of sizes. The region occupied by a large eddy can contain smaller eddies.

(4) *Dissipation:* momentum is transferred from larger to smaller eddies in an inviscid way, until velocity gradients become so large that the energy is dissipated by viscosity.

(5) *Diffusivity:* The chaotic motion enhances the rate of mixing and diffusion of momentum and heat compared to laminar flows.

2.2. Energy cascade and turbulent scales

As previously mentioned, turbulence can be understood as a process in which kinetic energy is transferred across a wide range of length scales (Fig. 2.1). This view was first proposed by Richardson (1922) [27], who introduced the concept of the *energy cascade*. In this framework, energy is injected at the largest scales of the flow, corresponding to eddies whose sizes are comparable to the width of the turbulent region. These large eddies are unstable and break down into smaller ones, passing energy downward through the cascade via inviscid mechanisms. As the eddy size ℓ decreases, viscous effects become increasingly important, and the cascade ultimately terminates at the smallest scales, where the Reynolds number $Re(\ell) = u(\ell)\ell/\nu$ is low enough for viscosity to dissipate the remaining energy. A quantitative theory describing these smallest scales was later developed by Kolmogorov (1941) [16].

His fundamental hypothesis is that, sufficiently far down the cascade and at high Reynolds numbers, the statistics of the small-scale motions become independent of the large-scale flow features. In particular, Kolmogorov postulated that the small scales are statistically isotropic and are fully characterized by only two parameters: the kinematic viscosity ν, and rate of kinetic energy dissipation per unit mass ε.

On dimensional grounds, this leads to the existence of a smallest characteristic length

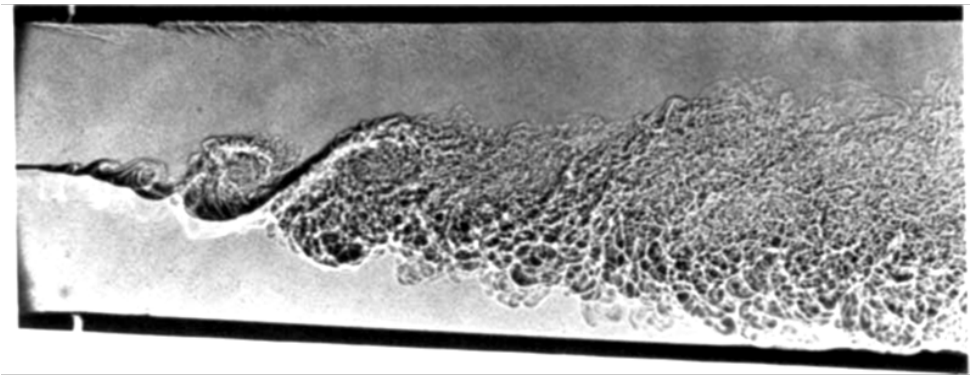

Figure 2.1: Visualization of eddy scales in a plane mixing layer. Large-scale structures dominate the initial region, while downstream evolution shows the development of smaller scale eddies. (from Brown and Roshko [6])

scale,

$$\eta = \left(\frac{\nu^3}{\varepsilon}\right)^{1/4} \tag{2.1}$$

now known as the *Kolmogorov microscale*.
The physical basis for this hypothesis is that, as energy is transferred through the cascade, not only is directional information lost, but so too is information about the geometry of the large eddies, which is set by the mean flow and boundary conditions. Consequently, the statistics of the smallest scales become universal, exhibiting similar behavior in all high-Reynolds-number turbulent flows. Small eddies are primarily advected by the velocity field of the larger eddies. As a result, small eddies do not interact directly with the mean flow or the large-scale structures and are therefore nearly isotropic.
These concepts can be summarized in the so-called **Kolmogorov's first similarity hypothesis** [26]:

> *In high Reynolds number turbulence the statistical properties of velocity at sufficiently small scales are universal and depend only on the mean energy dissipation rate ε and the kinematic viscosity ν.*

Kolmogorov further proposed a **second similarity hypothesis**, which concerns the range of scales lying between the large, energy-containing eddies of size l_0, comparable to the flow scale $\mathcal{L}$, and the smallest dissipative scales.

> *In high Reynolds number turbulence the statistical properties of velocity at scales in the range $\ell_0 \gg \ell \gg \eta$ are universal and depend only on the mean energy dissipation rate ε*

These scales form the *inertial subrange*. Eddies in this range are small compared with

the large-scale flow structures and insensitive to boundary conditions, yet large enough that viscous dissipation does not directly affect their dynamics. Energy is transferred conservatively through the inertial subrange from larger to smaller scales, with ε representing the constant flux of energy transferring toward the dissipative range. If there is no transport or production of kinetic energy then turbulence decays and ε can be defined as

$$\varepsilon(t) = -\frac{dk(t)}{dt}$$

where k is the turbulent kinetic energy per unit mass (Eq. 2.6).

A schematic representation of the different regions of the energy cascade proposed by Kolmogorov is shown in Fig. 2.3. The dissipation range and the inertial subrange together form the *universal equilibrium range*, which is common to all turbulent flows at sufficiently high Reynolds numbers. This range is separated from the energy-containing range, which depends on the specific flow configuration, by the characteristic length scale l_{EI} ($\ell_{\mathrm{EI}} = \frac{1}{6}\ell_0$), marking the transition between the energy-containing and inertial ranges. The transition between the inertial and dissipation ranges is characterized by the length scale l_{DI} ($\ell_{\mathrm{DI}} = 60\eta$).

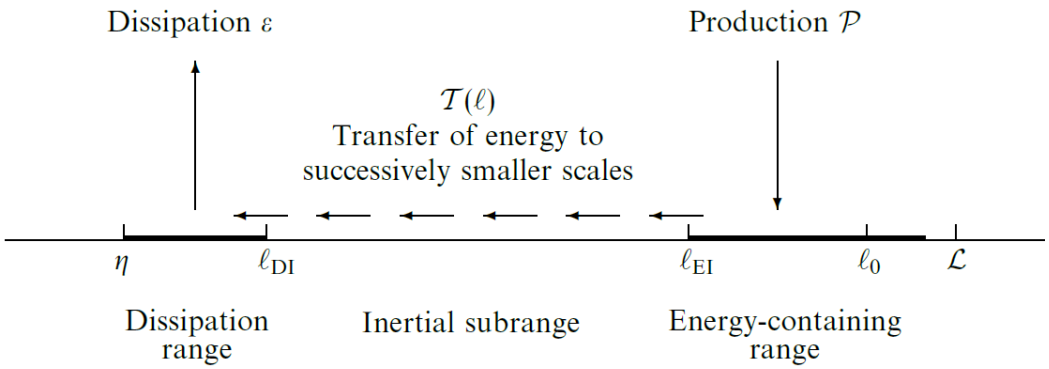

Figure 2.2: Schematic of the turbulent energy cascade in scale space for high Reynolds number flows. (from Pope [26])

2.3. Turbulence statistics and descriptors

Before proceeding with the modeling of the energy cascade, a statistical description of turbulence is provided. Due to its chaotic nature, a deterministic prediction of instantaneous quantities is practically impossible; thus, turbulence characterization relies on statistical descriptors rather than instantaneous values. In most engineering applications, only the global or averaged properties of turbulent flows are of interest, such as the intensity of

fluctuations and their characteristic spatial and temporal scales.

In principle, statistical quantities are defined as *ensemble averages* [17], obtained by repeating the same experiment under identical conditions and averaging the resulting flow realizations. Denoting by $u^m(\mathbf{x}, t)$ the m-th power of a random flow quantity measured in the n-th realization, the ensemble average is defined as

$$\langle \mathbf{u}^m(\mathbf{x}, t) \rangle = \lim_{N \to \infty} \frac{1}{N} \sum_{n=1}^{N} \mathbf{u}^m(\mathbf{x}, t : n). \tag{2.2}$$

In practice, performing a sufficiently large number of identical experiments is rarely feasible. A significant simplification is therefore achieved by assuming *statistical stationarity*, for which the statistical properties of the turbulent flow are independent of time. Under this assumption, ensemble averages can be replaced by time averages obtained from a single, sufficiently long measurement. Throughout this work, the operator $\langle \cdot \rangle$ will denote such time-averaged quantities.

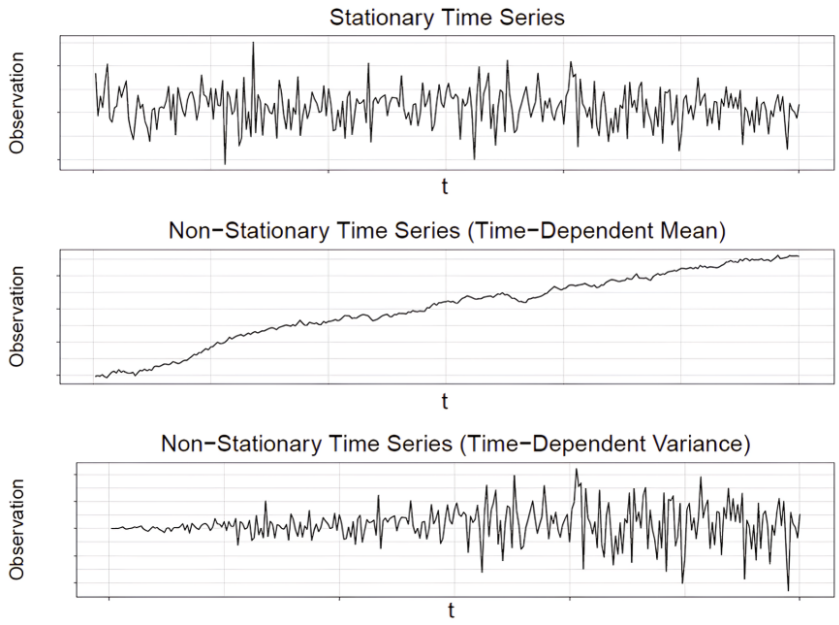

Figure 2.3: Example of stationary and non-stationary time series (adapted from Bauer [2]).

Once the averaging procedure has been defined, statistical moments of the velocity fluctuations can be introduced to quantify different physical aspects of turbulence. According to the *Reynolds decomposition* procedure, let the instantaneous velocity component be decomposed as follows:

$$\mathbf{u}(\mathbf{x}, t) = \langle \mathbf{u}(\mathbf{x}, t) \rangle + \mathbf{u}'(\mathbf{x}, t),$$

where $u'(t)$ is the fluctuating component with zero mean by construction, $\langle u'(t)\rangle = 0$.

The first statistical moment ($m = 1$) corresponds to the mean flow quantity $\langle u\rangle$ and represents the time-averaged velocity field.

$$\langle \mathbf{u}(\mathbf{x}, t)\rangle = \frac{1}{N}\sum_{n=1}^{N} \mathbf{u}(\mathbf{x}, t : n). \tag{2.3}$$

While this quantity characterizes the global flow behavior, it does not directly provide information about turbulent fluctuations. Such information is contained in the higher-order moments of the fluctuating component. The second moment ($m = 2$), given by the *variance* $\langle \mathbf{u}'^2\rangle$, provides a direct measure of the intensity of turbulent fluctuations. It is commonly expressed in terms of the *root-mean-square* value. Since the mean of $\mathbf{u}'$ is zero by definition the root-mean-square value is equal to the standard deviation:

$$u_{\text{rms}} = \sqrt{\langle \mathbf{u}'^2\rangle}, \tag{2.4}$$

which is used to define the turbulence intensity as

$$\text{Tu} = \frac{u_{\text{rms}}}{\langle \mathbf{u}\rangle}. \tag{2.5}$$

The second-order statistics are also directly related to the *turbulent kinetic energy*, defined for a three-dimensional velocity field as

$$k = \frac{1}{2}\langle \mathbf{u}'_i \mathbf{u}'_i\rangle \tag{2.6}$$

which represents the kinetic energy per unit mass associated with turbulent motions. These quantities are the main descriptors of turbulence and constitute the main inputs for CFD analysis and spectral studies.

Higher-order moments provide additional information on the statistical structure of turbulence. The third moment, commonly expressed through the *skewness*, characterizes the asymmetry of the probability distribution of velocity fluctuations, while the fourth moment, expressed as the *kurtosis* or flatness, quantifies the occurrence of rare, intense events and is often used as an indicator of intermittency. In homogeneous isotropic turbulence, described in the following section (2.4), skewness is expected to vanish and kurtosis approaches the Gaussian value of three. These higher-order statistics can provide qualitative indicators of isotropy and data quality.

Second-order moments such as the variance quantify the intensity of turbulent fluctua-

tions, but they provide no information about the spatial or temporal organization of the turbulent motion. To address this limitation, it is therefore necessary to introduce statistical measures that describe how velocity fluctuations are correlated in space or time. The main descriptor in this sense is the *autocorrelation function* R_{uu}, which measures the correlation between the same fluctuating quantity as the spatial separation or time lag increases [13, 17, 26].

In general, two forms of autocorrelation can be defined. The *spatial autocorrelation* describes how velocity fluctuations measured at two distinct spatial locations are correlated as a function of their separation distance. This formulation is relevant for the description of turbulent structures in physical space and forms the basis for theoretical energy spectrum models. For this reason, spatial autocorrelation is discussed in more detail in Section 2.5.

On the other hand, the *temporal autocorrelation* characterizes the correlation of velocity fluctuations at a fixed spatial location as a function of the time lag between measurements. In this study, velocity measurements are obtained using hot-wire anemometry, which provides time-series of the velocity components. Consequently, temporal autocorrelation functions are employed in the post-processing of experimental data.

For a statistically stationary turbulent flow at a fixed location, the temporal autocorrelation function of a velocity component $\mathbf{u}'(t)$ is defined as

$$R_{uu}(\tau) = \langle \mathbf{u}_i'(t)\mathbf{u}_i'(t+\tau)\rangle, \tag{2.7}$$

where τ is the time lag between two measurements of $u'(t)$. The autocorrelation function is more frequently considered in its normalized form, denoted as the autocorrelation coefficient.

$$\rho(\tau) = \frac{\langle \mathbf{u}_i'(t)\mathbf{u}_i'(t+\tau)\rangle}{\langle \mathbf{u}_i'^2\rangle} \tag{2.8}$$

The autocorrelation is maximum when the two time arguments $\mathbf{u}'(t)$ are equal ($\rho(0) = 1$), is symmetric with respect to τ and decreases with increasing time lag as $\mathbf{u}'(t)$ gradually loses correlation with itself until eventually $\rho(\tau) = 0$. From the autocorrelation coefficient it is possible to obtain the integral timescale $\mathcal{T}$ of the process, which measures the characteristic lifetime of the largest eddies. It can be defined as the "memory" of turbulence as it represents the time for which a particle is influenced by its previous velocity.

$$\mathcal{T} = \int_0^\infty \rho(\tau)\, d\tau, \tag{2.9}$$

Measurements are, however, usually taken for a duration much longer than the time lag for which $\rho(\tau) = 0$, therefore the integration is generally performed until the first zero-crossing, meaning until the time lag $\tau*$ at which the autocorrelation coefficient first becomes zero ([13] Eq. 1-84).

By applying Taylor's frozen turbulence hypothesis (Eq. 2.22), which serves as a link between spatial and temporal quantities, as discussed in more detail in Section 2.5, then the characteristic length scale of the most energetic eddies, the integral length scale Λ can be obtained. Considering only the streamwise fluctuation, the longitudinal integral length scale is given by:

$$\Lambda_x = U\mathcal{T} = U \int_0^{\tau*} \rho(\tau)\, d\tau \tag{2.10}$$

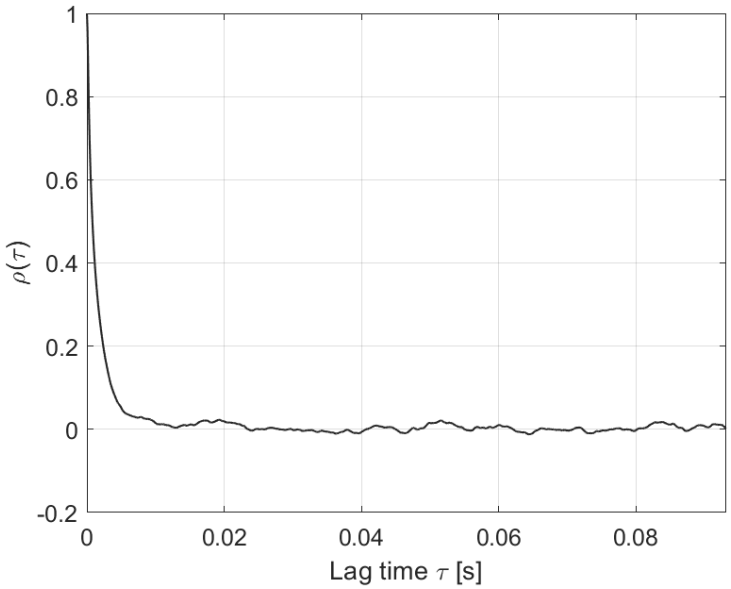

Figure 2.4: Autocorrelation coefficient from hot-wire measurements

2.4. Homogeneous isotropic turbulence

The statistical framework introduced in the previous section provides the tools to study and quantify turbulence. To obtain a quantitative description of the energy cascade presented in Kolmogorov's 1941 theory (K41) [16], it is necessary to adopt a fundamental assumption that greatly simplifies the mathematical formulation. This assumption is that of homogeneous and isotropic turbulence (HIT), under which turbulence statistics are invariant with respect to spatial position and direction. Homogeneity implies uniformity throughout the flow field, while isotropy requires the absence of any preferred direction, such that the statistical features of the turbulence are identical in all orientations [21]. As a result, velocity correlations do not depend on position and, therefore, it is possible to define a direct connection between statistical quantities and their spectral representation through Fourier transformation.

In HIT, either no mean flow is present or the mean velocity is spatially uniform, allowing the turbulence to be analyzed in a reference frame moving with the mean flow. As a consequence, no mean velocity gradients or average shear stresses exist, and there is no direct mechanism for the continuous production of turbulent kinetic energy through mean-flow instabilities. Homogeneous turbulence is therefore typically *decaying*, with energy of the large scales flowing to the smaller ones through the Kolmogorov cascade. In contrast, when a gradient of the mean velocity is present, an average shear stress necessarily arises and the turbulence becomes anisotropic. Such flows are commonly referred to as *shear-flow turbulence*, a class that includes wall-bounded turbulence and anisotropic free turbulence.

Although perfectly homogeneous and isotropic turbulence does not occur in most practical flows, it can be approximated in direct numerical simulations performed in periodic domains or, as in this study, in controlled laboratory experiments such as grid-generated turbulence. HIT represents the simplest form of turbulence and serves as a fundamental model for investigating its universal features. In light of Kolmogorov's similarity hypotheses, this idealization becomes increasingly relevant at sufficiently small scales and high Reynolds numbers, where the influence of large-scale anisotropy diminishes and turbulence approaches local isotropy.

Beyond its physical relevance, the assumption of homogeneity and isotropy also leads to important simplifications in the statistical description of turbulence. In general, the Reynolds-averaged Navier–Stokes equations are not closed, since the Reynolds stress tensor introduces additional unknowns that cannot be expressed solely in terms of mean-flow quantities. However, if the turbulent fluctuations are perfectly isotropic, the Reynolds stress tensor simplifies significantly: the off-diagonal components vanish and the normal

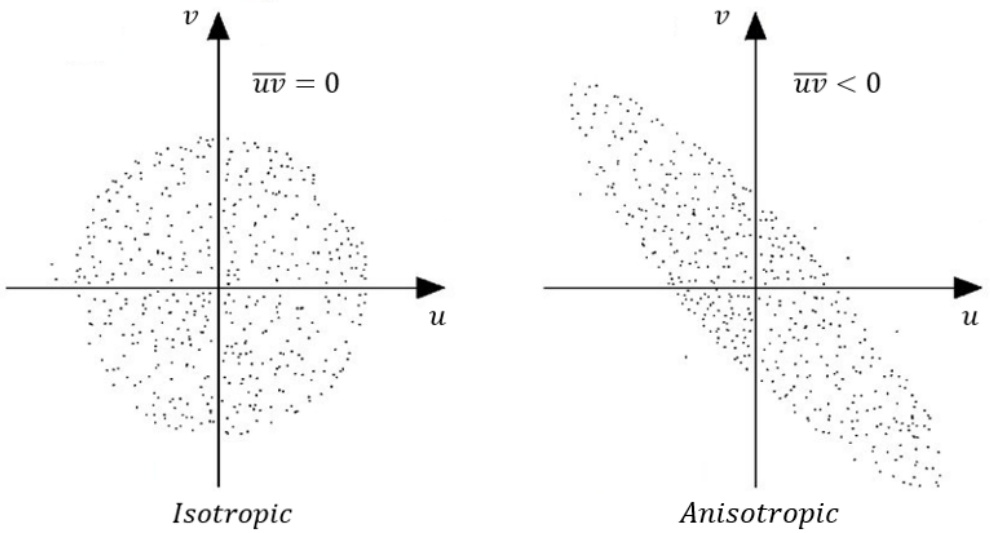

Figure 2.5: Scatter diagrams showing instantaneous velocity fluctuations in isotropic and anisotropic 2D turbulent fields (from Kundu, Cohen, Dowling [17]).

stresses become equal: $\langle \mathbf{u}_1'^2 \rangle = \langle \mathbf{u}_2'^2 \rangle = \langle \mathbf{u}_3'^2 \rangle$. In this case, no directional preference exists in the fluctuating velocity field, and correlations such as $\langle uv \rangle$ are zero. As a result of isotropy, the turbulent kinetic energy can be written as

$$k(t) = \frac{3}{2} \langle \mathbf{u}_i'(t)^2 \rangle \tag{2.11}$$

This behavior may be visualized by considering the joint distribution of velocity fluctuations in different directions as shown in Fig. 2.5. In isotropic turbulence, instantaneous velocity components are symmetrically distributed, so that positive and negative fluctuations occur with equal probability in all directions. In contrast, anisotropic turbulence, such as that found in shear flows, exhibits oriented correlations between velocity components, resulting in nonzero shear stresses. When homogeneity is additionally satisfied, turbulence statistics are spatially invariant and all directions are equivalent. Comprehensive discussions of homogeneous isotropic turbulence may be found in classical references such as Batchelor [1] and Hinze [13].

2.5. The energy spectrum

The transfer of energy along the cascade occurs across scales rather than through specific spatial locations. As a result, a central question in turbulence theory is not the physical location of energy, but how much kinetic energy is associated with eddies of a given size.

To address this question, it is natural to decompose the velocity field into contributions corresponding to different length scales. This decomposition is most conveniently performed in *wavenumber space*, a spectral representation of the flow in terms of spatial frequencies of turbulent fluctuations.
Instead of describing the turbulent velocity field $\mathbf{u}(\mathbf{x}, t)$ as a function of position, it is expressed in terms of its Fourier components associated with a wavenumber vector $\boldsymbol{\kappa}$ [26]. The wavenumber magnitude is defined as $\kappa = |\boldsymbol{\kappa}| = 2\pi/\ell$, meaning that small κ corresponds to large-scale eddies, while large κ corresponds to small-scale fluctuations.
The velocity field may therefore be written as

$$\mathbf{u}(\mathbf{x}, t) = \int \hat{\mathbf{u}}(\boldsymbol{\kappa}, t) e^{i\boldsymbol{\kappa}\cdot\mathbf{x}} d\kappa \tag{2.12}$$

The spatial structure of turbulence in the physical space is described by the *two-point correlation* R_{ij} [33], defined for two points separated by the vector $\mathbf{r}$ as

$$R_{ij}(\mathbf{x}, \mathbf{r}, t) = \langle u_i'(\mathbf{x}, t) u_j'(\mathbf{x} + \mathbf{r}, t) \rangle \tag{2.13}$$

For homogeneous turbulence R_{ij} does not depend on absolute position $\mathbf{x}$, but only on the separation vector $\mathbf{r}$. As a result, all regions of the flow share the same statistical properties, and R_{ij} admits a global Fourier transform.
When the separation vector is set to zero, $\mathbf{r} = 0$, the two-point correlation tensor reduces to the Reynolds stress tensor $\langle u_i u_j \rangle$ with $i, j = 1, 2, 3$. Its diagonal components ($i = j$) represent the variances of the velocity components, such as $\langle \mathbf{u}_1^2 \rangle$, $\langle \mathbf{u}_2^2 \rangle$, and $\langle \mathbf{u}_3^2 \rangle$, which quantify the turbulence intensity in each direction. The off-diagonal components ($i \neq j$) correspond to the Reynolds shear stresses. In particular, setting $\mathbf{r} = 0$ allows the total turbulent kinetic energy to be obtained as

$$k = \frac{1}{2} \langle \mathbf{u}_i' \mathbf{u}_i' \rangle = \frac{1}{2} R_{ii}(0, t) \tag{2.14}$$

While this expression provides the total kinetic energy, it does not indicate how this energy is distributed across different length scales. To obtain this information, it is necessary to move to the spectral domain by considering the three-dimensional Fourier transform of the two-point correlation tensor. This transform defines the *velocity spectrum tensor* $\Phi_{ij}(\boldsymbol{\kappa}, t)$. For homogeneous turbulence, R_{ij} and Φ_{ij} form a Fourier transform pair, implying that the statistical information contained in physical space correlations can be equivalently

represented in wavenumber space:

$$\Phi_{ij}(\boldsymbol{\kappa}, t) = \frac{1}{(2\pi)^3} \iiint_{-\infty}^{\infty} e^{-i\boldsymbol{\kappa}\cdot\mathbf{r}} R_{ij}(\mathbf{r}, t) \mathrm{d}\mathbf{r}, \tag{2.15}$$

$$R_{ij}(\mathbf{r}, t) = \iiint_{-\infty}^{\infty} e^{i\boldsymbol{\kappa}\cdot\mathbf{r}} \Phi_{ij}(\boldsymbol{\kappa}, t) \mathrm{d}\boldsymbol{\kappa}, \tag{2.16}$$

The tensor $\Phi_{ij}(\boldsymbol{\kappa}, t)$ describes how velocity correlations are distributed among different wavenumbers. In isotropic turbulence, however, the statistical properties of the flow are independent of direction, and the energy depends only on the magnitude $\kappa = |\boldsymbol{\kappa}|$. It is therefore convenient to introduce the *three-dimensional energy spectrum* $E(\kappa, t)$, a scalar function representing the distribution of kinetic energy over wavenumber magnitude.
The energy spectrum is obtained by integrating the trace of the velocity spectrum tensor over the surface $S(\kappa)$ of a spherical shell of radius κ in wavenumber space:

$$E(\kappa, t) = \oint \frac{1}{2} \Phi_{ii}(\boldsymbol{\kappa}, t) \, \mathrm{d}\mathcal{S}(\kappa) \tag{2.17}$$

This operation removes directional information and is valid under the assumption of isotropy; in anisotropic flows, energy is not uniformly distributed over the spherical shell. This scalar function $E(\kappa, t)$ represents the energy density per unit wavenumber, such that the integral of $E(\kappa, t)$ from 0 to ∞ yields the total kinetic energy $k(t)$.

$$k(t) = \int_0^{\infty} E(\kappa, t) \, d\kappa \tag{2.18}$$

Similarly, the turbulent dissipation rate $\varepsilon(t)$ is related to the energy spectrum through a weighted integral that accounts for viscous effects. Because dissipation primarily occurs at the smallest scales (highest wavenumbers), the spectrum is weighted by $2\nu\kappa^2$:

$$\varepsilon(t) = \int_0^{\infty} 2\nu\kappa^2 E(\kappa, t) d\kappa \tag{2.19}$$

This relationship, derived from the velocity gradients of the flow field, identifies $2\nu\kappa^2 E(\kappa, t)$ as the dissipation spectrum.
A log-log representation of $E(\kappa)$ allows a clear visualization of the three regions of the energy cascade.

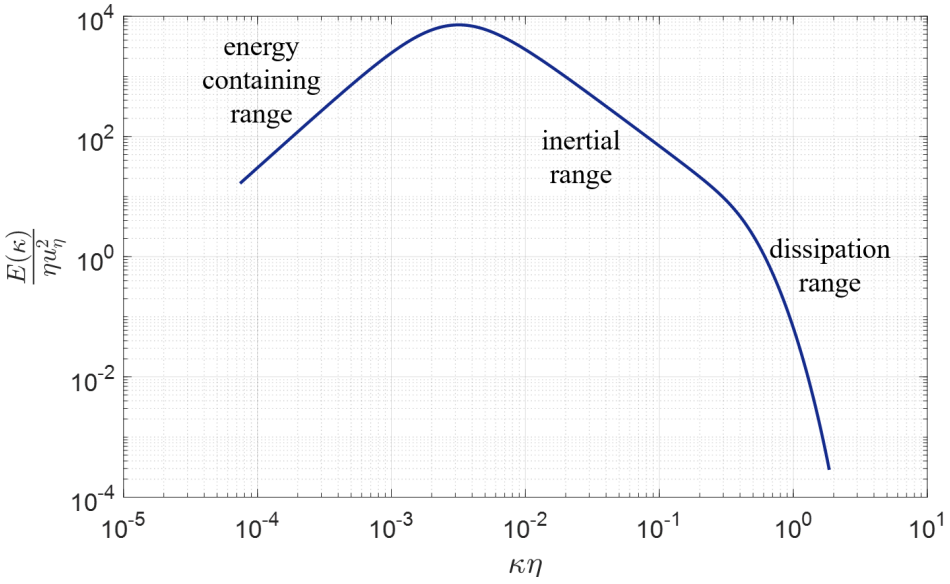

Figure 2.6: non-dimensional 3D turbulent energy spectrum plotted on a logarithmic scale (from Boufidi [4]).

Apart from time-resolved stereoscopic particle image velocimetry (TR-SPIV) or complex multi-probe hot-wire configurations, no experimental technique can directly measure the three-dimensional energy spectrum. Even for PIV-based approaches, this capability is limited to a few carefully controlled cases, since the finite inertia of the tracer particles acts as a spatial and temporal filter, attenuating high frequency and small scale fluctuations. As a result, many studies of turbulent velocity fields are confined either to numerical approaches such as DNS and LES, or experimentally to one- or two-dimensional measurements. A proper interpretation of experimental data therefore requires the introduction of the one-dimensional energy spectrum.

The one-dimensional longitudinal energy spectrum of the streamwise velocity component u_1 along the x_1 direction, denoted $E_{11}(\kappa_1)$, is the spectrum typically obtained from a line measurement, such as that provided by a hot-wire anemometer. It is defined as

$$\langle \mathbf{u}_1'^2 \rangle = \int_0^\infty E_{11}(\kappa_1)\, d\kappa_1, \tag{2.20}$$

Where κ_1 is the wavenumber associated with spatial variations along x_1.

In homogeneous turbulence, $E_{11}(\kappa_1)$ represents the distribution of kinetic energy among streamwise wavenumbers obtained from a line measurement, and corresponds to a projection of the three-dimensional energy spectrum onto the measurement direction. The one- and three-dimensional energy spectra are related through isotropic relations, which are

strictly valid only for isotropic turbulence. One relation, derived by Pope [26] Eq. 6.216,

$$E_{11}(\kappa_1) = \int_{\kappa_1}^{\infty} \frac{E(\kappa)}{\kappa} \left(1 - \frac{\kappa_1^2}{\kappa^2}\right) d\kappa \tag{2.21}$$

$E_{11}(\kappa_1)$ is a monotonically decreasing function of κ_1, and hence is maximum at $\kappa_1 = 0$.

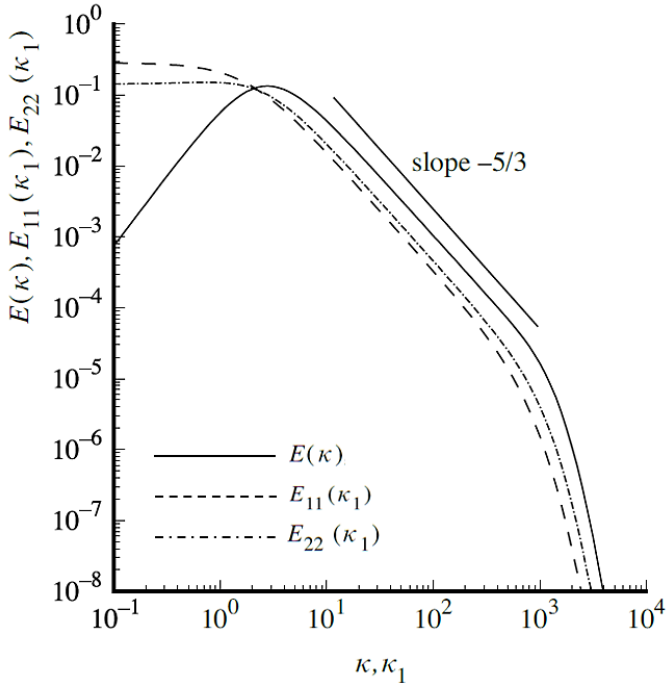

Figure 2.7: Comparison of 1D and 3D energy spectra in isotropic turbulence according to Pope's spectrum model (Section 2.5.1, Pope [26]).

Since the velocity measurements are acquired at a fixed spatial location and are time-resolved, the experimentally accessible spectrum is naturally defined in the temporal (frequency) domain rather than in the spatial (wavenumber) domain. The connection between these two descriptions is provided by *Taylor's frozen turbulence hypothesis* [32], which relates spatial and temporal fluctuations.

Taylor's hypothesis states that turbulent structures are transported past a measurement sensor by the mean flow while undergoing minimal change during this transport. With this assumption, the turbulence is treated as effectively "frozen" and carried downstream at a speed equal to the mean velocity U , which is assumed here to be aligned with the x_1 direction. As a result, spatial variations along the streamwise direction can be deduced from temporal measurements according to

$$x_1 = Ut \tag{2.22}$$

The corresponding relationship between the streamwise wavenumber κ_1 and the temporal frequency f is then given by

$$\kappa_1 = \frac{2\pi f}{U} \tag{2.23}$$

Using this transformation, the theoretically defined spatial energy spectrum can be related to the experimentally measured frequency spectrum as

$$E_{11}(f) = \frac{2\pi}{U} E_{11}(\kappa_1) \tag{2.24}$$

Taylor's frozen turbulence hypothesis is applicable to statistically stationary flows in which $\frac{u}{U} \ll 1$ so that the advection by the mean flow dominates over turbulent evolution. In isotropic and homogeneous flow, such as grid-generated turbulence, the approximation has been shown to be highly accurate for a wide range of turbulence statistics, including energy spectra. Inaccuracies may arise in flows with strong shear or significant unsteadiness.

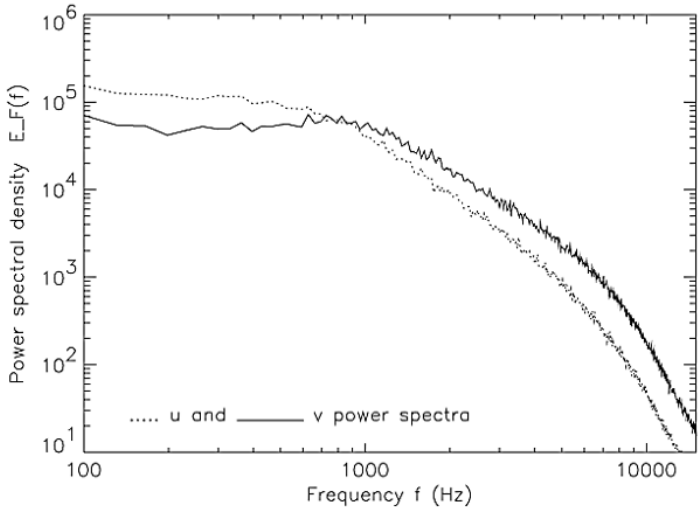

Figure 2.8: Hot-wire measurements of one-dimensional longitudinal and transversal velocity spectra (from Lewalle [18]).

2.5.1. Energy spectrum models

While integrating the spectral tensor $\Phi_{ii}(\boldsymbol{\kappa}, t)$ over a spherical shell gives the formal mathematical definition of the energy spectrum $E(\kappa)$, this definition alone does not indicate how energy is actually distributed across scales. To address this, it is necessary to consider the physics of the turbulent energy cascade, as described by Kolmogorov's similarity hypotheses. One of Kolmogorov's main results is the well-known $-5/3$ scaling of the energy spectrum in the inertial subrange, which follows from simple dimensional considerations.

According to the second similarity hypothesis, in the inertial subrange of high-Reynolds-number turbulence the energy transfer is independent of viscosity and depends only on the mean dissipation rate ε. The energy spectrum can therefore be assumed to depend only on ε and the wavenumber κ. Using the dimensions

$$E(\kappa) \sim L^3T^{-2}, \varepsilon \sim L^2T^{-3}, \kappa \sim L^{-1}$$

it follows directly that

$$E(\kappa) \propto \varepsilon^{2/3}\kappa^{-5/3} \tag{2.25}$$

Experimental results show that the proportionality constant C is approximately equal to 1.5.
Considering the one-dimensional spectra, the power-law exponent $-5/3$ remains the same for all three components, while the corresponding constants C_1 and C_2 are related to C. Specifically, $C_1 = \frac{18}{55}C$ for E_{11} and $C_2 = \frac{24}{55}C$ for E_{22}.

While Kolmogorov's $-5/3$ law provides an accurate representation of the energy spectrum within the inertial subrange, it does not account for the behavior of the spectrum in the energy-containing range or in the dissipation range. To address this limitation, Pope [26] proposed a model for the full energy spectrum, extending the inertial-range law to cover all relevant scales (Fig. 2.7).

$$E(\kappa) = C\varepsilon^{2/3}\kappa^{-5/3}f_L(\kappa\Lambda)f_\eta(\kappa\eta), \tag{2.26}$$

In this formulation, the $-5/3$ scaling is retained within the inertial subrange, while non-dimensional functions are introduced to describe the spectrum at the boundaries of the inertial range and are defined as:

$$f_L(\kappa\Lambda) = \left(\frac{\kappa\Lambda}{[(\kappa\Lambda)^2 + c_L]^{(1/2)}}\right)^{(5/3+p_0)} \tag{2.27}$$

$$f_\eta(\kappa\eta) = \exp\left(-\beta([(\kappa\eta)^4 + c_\eta^4]^{1/4} - c_\eta)\right) \tag{2.28}$$

where Λ and η represent the integral and Kolmogorov length scale.

The function f_L shapes the energy-containing range and tends to unity for high wavenumbers, while f_η models the dissipation range and tends to unity for low wavenumbers. In the inertial subrange, both functions are equal to one, allowing the energy spectrum to take the classical Kolmogorov's $-5/3$ form.
β and p_0 are empirical constants, with values $\beta = 5.2$ and $p_0 = 2$. In particular, p_0

determines the slope of the spectrum in the energy-containing region. The coefficients c_L and c_η depend on the kinetic energy k, dissipation rate ε, and viscosity ν of the flow, and are chosen such that Eqs. (2.18) and (2.19) are satisfied. For high–Reynolds-number flows, commonly accepted values are $c_L \approx 6.78$ and $c_\eta \approx 0.40$ [26].

In contrast to the Pope spectrum, which is parametric and requires tuning of constants, the *von Kármán spectrum* represents an analytical and universal formulation of isotropic turbulence, with constants determined analytically.
Originally proposed by von Kármán [35], this model was one of the first to incorporate the Kolmogorov's $-5/3$ scaling within a single analytical expression. It is meant to connect the energy-containing range which, from theory, obeys a κ^4 power law at low wavenumbers, with the Kolmogorov's inertial subrange law.

The von Kármán energy spectrum is given by (Hinze [13] Eq. 3-154)

$$E(\kappa) = \frac{55}{9\sqrt{\pi}} \frac{\Gamma(5/6)}{\Gamma(1/3)} \frac{\langle \mathbf{u}'^2 \rangle}{\kappa_e} \frac{(\kappa/\kappa_e)^4}{[1 + (\kappa/\kappa_e)^2]^{17/6}} \tag{2.29}$$

where κ_e is the wavenumber of the largest eddies and is defined as [10]:

$$\kappa_e = \frac{\sqrt{\pi}}{\Lambda} \frac{\Gamma(5/6)}{\Gamma(1/3)} \tag{2.30}$$

The Pope spectrum recovers the von Kármán form as a special case by setting the large-scale exponent $p_0 = 4$ and fixing the constant c_L to the analytical value given by a ratio of Gamma functions, which are numerical constants with specific values (approximately $\Gamma(5/6) \approx 1.13$ and $\Gamma(1/3) \approx 2.68$). These constants arise from the analytical normalization of the spectrum to ensure that the integral of $E(\kappa)$ recovers the total kinetic energy, as required by Eq. (2.18).
In addition, the dissipative correction function is set to unity, as the von Kármán formulation does not model the dissipation range.
The resulting spectrum therefore exhibits a universal and idealized shape in which the spectral form is fully defined by analytical constants rather than numerical tuning. This universality has made the von Kármán spectrum one of the most widely used models for isotropic turbulence, particularly in applications such as wind-tunnel experiments.

In this thesis, the experimental spectrum is compared with the idealized von Kármán spectrum and, additionally, with the Pope spectrum, in order to validate the results obtained using the von Kármán formulation. To enable this comparison, the three-dimensional

von Kármán energy spectrum must first be reduced to its one-dimensional form and then transformed into the frequency domain, which corresponds to the domain of the experimental measurements.
The one-dimensional spectrum is obtained from the three-dimensional formulation (Eq. 2.29) by applying the standard relation between one- and three-dimensional isotropic spectra (Eq. 2.21). This procedure results in ([10] Eq. E.19)

$$E_{11}(\kappa_1, t) = \frac{2}{\sqrt{\pi}} \frac{\Gamma\left(\frac{5}{6}\right)}{\Gamma\left(\frac{1}{3}\right)} \frac{\langle \mathbf{u}'^2 \rangle}{\kappa_e} \left[1 + \left(\frac{\kappa_1}{\kappa_e}\right)^2\right]^{-5/6} \tag{2.31}$$

By substituting the definition of the wavenumber κ_e (Eq. 2.30) and applying Taylor's frozen turbulence hypothesis (Eqs. 2.24 and 2.23), the one-dimensional von Kármán spectrum can be expressed in the frequency domain. This form [3] will be employed throughout the thesis to compute the streamwise component of the integral length scale Λ_x:

$$E_{11}(f) = \frac{4\langle \mathbf{u}'^2 \rangle \Lambda_x}{U} \left(1 + \left(\frac{8\pi f \Lambda_x}{3U}\right)^2\right)^{-5/6} \tag{2.32}$$

Conventionally, the integral length scale Λ_x is estimated from the low-frequency limit of $E_{11}(f)$. Taking the limit $f \to 0$ [28]:

$$\Lambda_x = \left[\frac{E_{11}(f)\, U}{4\langle \mathbf{u}'^2 \rangle}\right]_{f \to 0} \tag{2.33}$$

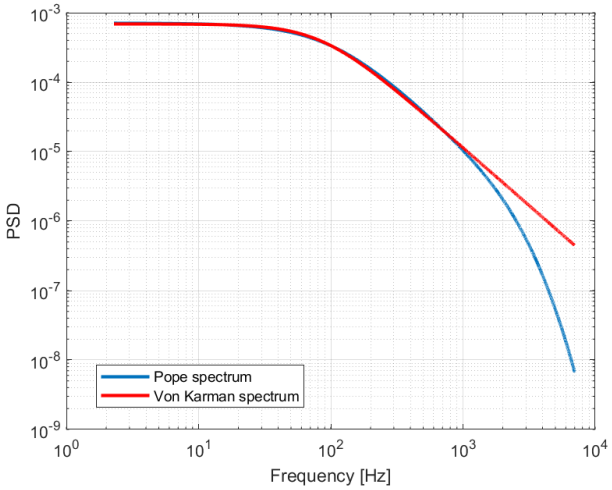

Figure 2.9: von Kármán and Pope spectra under identical flow conditions.

3| Experimental setup

The present chapter provides an overview of the study facility, the instrumentation used, and the methodologies applied for data processing.

3.1. The VKI C-1 wind tunnel

The experimental data presented in this thesis are obtained in the C-1 Low-Speed Cascade Wind Tunnel at the von Kármán Institute for Fluid Dynamics. A schematic of the facility is shown in Figure 3.1 [34].

The C-1 rig is a continuous-flow, open-circuit wind tunnel designed for detailed studies of aerodynamic flow structures in turbomachinery cascades. Airflow is generated by a centrifugal fan driven by a DC motor, allowing precise control of the flow velocity and maintaining the desired Reynolds number during experiments.

Upstream of the test section, the air passes through a diffuser followed by three wire-mesh screens located within an accessible settling chamber. The flow then enters a convergent nozzle equipped with an additional mesh screen, which improves flow uniformity. The test section is located downstream of the nozzle and has a rectangular cross-section with a height of 127 mm and a width of 500 mm. It includes both the turbulence grid and the linear cascade assembly. Downstream of the test section, the airflow is discharged directly to the atmosphere.

The cascade is mounted between two large circular rotating sidewalls, allowing adjustments of the inlet flow incidence angle. Two adjustable tailboards are installed downstream of the cascade to guide the outlet flow and tailor periodicity. The facility is also equipped with a boundary-layer suction system consisting of slots located on the sidewalls upstream of the cascade and connected to an auxiliary exhauster driven by a DC motor. During the present experimental campaign, the system was operated in a passive mode, as this configuration has proven effective in removing the boundary layer close to the walls while ensuring an axial velocity density ratio ($AVDR = (\rho V_x)_{out}/(\rho V_x)_{in}$), used

to assess mass-flow balance and periodicity in cascade experiments, close to unity. Any further increase in the suction rate was avoided, as it could have significantly affected flow periodicity and inlet incidence without providing a clear improvement in the endwall boundary-layer topology.

The test section includes multiple access slots for monitoring flow quantities such as pressure and temperature using both fixed and traversable instrumentation as well as a Particle Image Velocimetry (PIV) optical access. Two independent two-axis traversing systems, allowing pitchwise and spanwise movement, are available to position measurement probes in planes located upstream and downstream of the cascade, respectively. These traversing systems are actuated by four electric motors and controlled remotely from the facility control station.

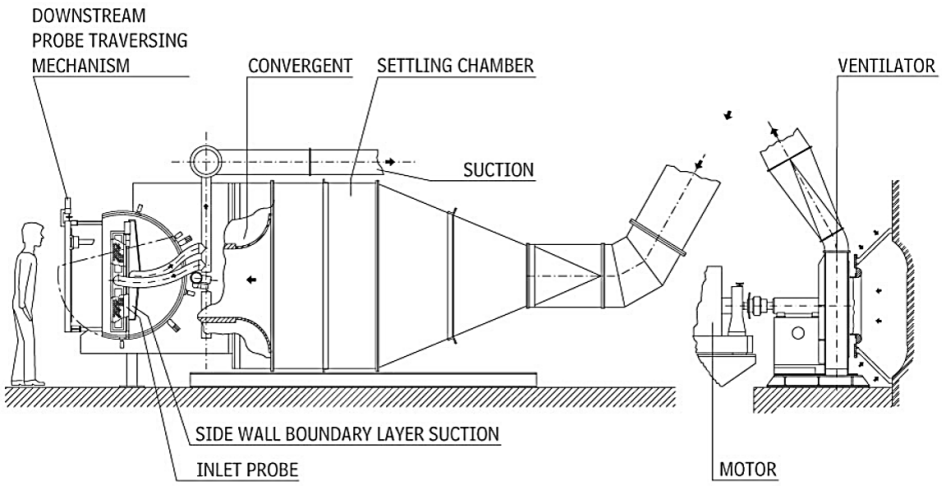

Figure 3.1: Illustration of the C-1 facility

3.2. The SPLEEN C1 cascade

The blade tested in the present study is a low-speed rescaling of the SPLEEN C1 blade, a geometry originally conceived to be representative of a high-speed low-pressure turbine. This type of turbine component is part of modern geared turbofans, which can reach bypass ratios higher than 10, thus achieving great reductions in specific fuel consumption. In such engines, the low-pressure turbine is among the most critical components, as it operates at transonic Mach numbers, exceeding Mach numbers 0.8 at the outlet [19], and low Reynolds numbers, conditions that strongly affect boundary layer state, promoting transition and potential separation. The present experimental campaign is conducted within the framework of the EU-funded HE-ART project and represents a follow-up of

the original SPLEEN project. Its main objective is to obtain detailed boundary layer data on the SPLEEN C1 blade and to characterize its behavior to varying free-stream turbulence levels, with the aim of improving the understanding of transition and separation mechanisms under engine-representative loading. To preserve representativity of the high-speed flow physics in low-speed conditions, the first step of the campaign consisted in rescaling the original transonic SPLEEN C1 geometry to low-speed conditions while maintaining the blade loading and pressure gradients that mostly affect boundary layer development.

This was achieved through an aerodynamic scaling methodology based on matching the pressure coefficient distribution of the high-speed blade, rather than relying on kinematic similarity. A detailed description of the rescaling procedure can be found in [25], while the resulting geometrical parameters of the low-speed cascade are reported in Fig. 3.2.

Figure 3.2: Low-speed SPLEEN C1 blade geometry (from Pastorino et al. [25])

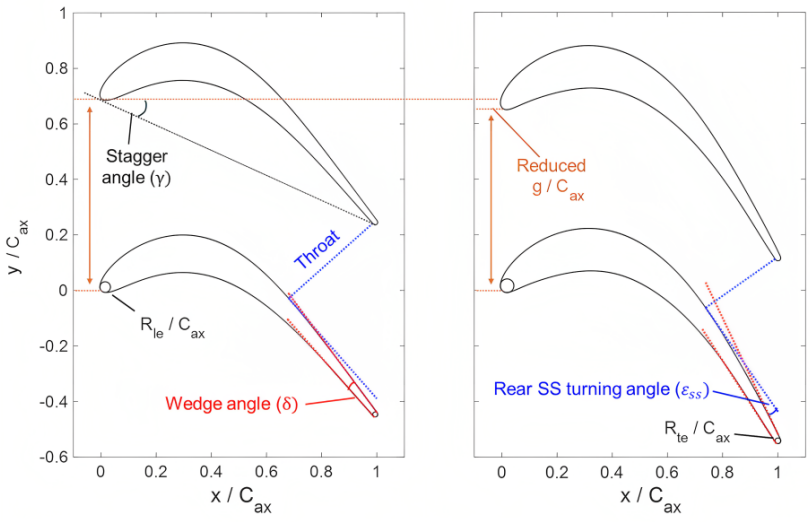

Quantity	Value	Unit
α_1	37.0	deg
α_2	61.5	deg
γ	28.4	deg
C_{ax}	62.1	mm
C_h	70.9	mm
g/C_{ax}	0.658	–
$t_{\mathrm{max}}/C_{\mathrm{ax}}$	15.3	%
$R_{\mathrm{LE}}/C_{\mathrm{ax}}$	2.46	%
$R_{\mathrm{TE}}/C_{\mathrm{ax}}$	1.02	%
o/C_{ax}	0.307	–
δ	7.4	deg
$\varepsilon_{\mathrm{ss}}$	9.4	deg

3.3. Turbulence generators

To characterize and control the inlet free-stream turbulence for the present experimental campaign, two turbulence grids were employed upstream of the cascade, mounted normal to the incoming flow. The grids are based on the jet-grid concept and consist of parallel arrays of circular rods with different diameters, while sharing the same solidity, defined as the fraction of blocked area, in order to have equal pressure losses across the device.

The grids were designed and experimentally characterized in a previous study conducted at the von Karman Institute by Bertelli et al. [3] with the objective of generating a wide

range of homogeneous and nearly isotropic free-stream turbulence while also allowing independent control of turbulence intensity and integral length scale. An illustration of their geometry is provided in Fig. 3.3.
In the present work, the grids were operated both in passive mode, corresponding to zero jet injection, and in active mode through controlled upstream and/or downstream air injection.

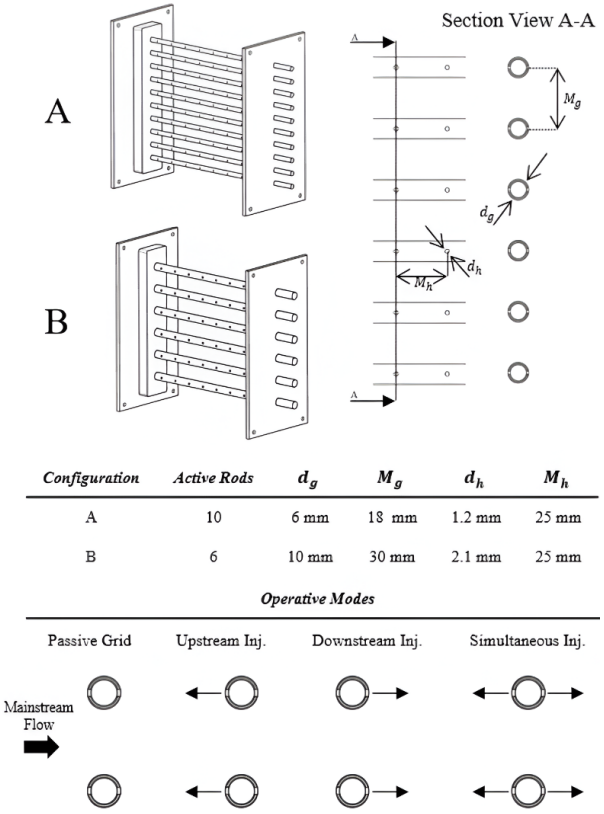

Figure 3.3: Turbulence grids geometry (from Bertelli et al. [3])

The use of turbulence generating grids is well established in experimental aerodynamics, where passive grids are commonly employed to generate nearly homogeneous and isotropic turbulence from an initially uniform flow with low background turbulence levels [28]. In such configurations, turbulence is produced through flow blockage and the interaction of bar wakes, resulting in repeatable flow conditions. However, while passive grids are effective in setting turbulence intensity levels, they offer limited control over the turbulence length scales, which are imposed by the grid geometry.

Jet grids, on the other hand, generate turbulence through the combined effect of passive grid blockage and bar wakes and distributed jet injections interacting with those wakes. Jet injection allows higher turbulence intensities than passive grids alone and modification

of turbulence spectra. The peculiarity of the grids employed in this campaign is the range of control of length scales while maintaining good homogeneity and low pressure loss.

The grids were initially characterized in passive mode using hot-wire measurements, with the grid positioned at different streamwise locations upstream of the cascade leading edge. The distance between the grid and the leading edge was adjusted through a sliding support system: the grid was mounted on a sliding metal base and displaced using a pulling bar. By moving the grid to different streamwise positions, various free-stream turbulence conditions were generated.

After the passive mode testing, the grids were operated in active mode by supplying compressed air individually to each grid rod. High pressure air was drawn from the Von Karman 40 bar supply line and first routed through a mass flow meter based on the choking principle (Fig. 3.4a), using interchangeable critical orifices of different sizes. When choked conditions are achieved across the orifice, the injected mass flow rate can be determined from the choked flow relation Eq. 3.1:

$$\dot{m}_h = \frac{AP_0}{\sqrt{T_0}}\sqrt{\frac{\gamma}{R}}\,M\left[1+\frac{\gamma-1}{2}M^2\right]^{-\frac{\gamma+1}{2(\gamma-1)}} \tag{3.1}$$

where the Mach number $M = 1$ and A is the cross section of the orifice.
The flow was then delivered to the grid through a feeding system consisting of a main supply line connected to a plenum (Fig. 3.4b), from which individual tubes feeding each grid rod departed. The plenum was located inside the settling chamber, while the feeding tubes were directed through the mesh screen in the test section and guided along the wind tunnel sidewall to minimize interference with the incoming flow.
Reliable and repeatable measurement of the injected air mass flow rate is necessary to compute the injection ratio, which characterizes the different active operating modes of the grid. Variations of the injection ratio allow different turbulence conditions to be generated, and the mass flow measurements were therefore used to build injection ratio curves for the active grid operation. The injection ratio is defined as follows:

$$J = \frac{\dot{m}_h}{\dot{m}} \tag{3.2}$$

where $\dot{m}_h$ indicates the injected mass flow and $\dot{m}$ the total mass flow in the facility.

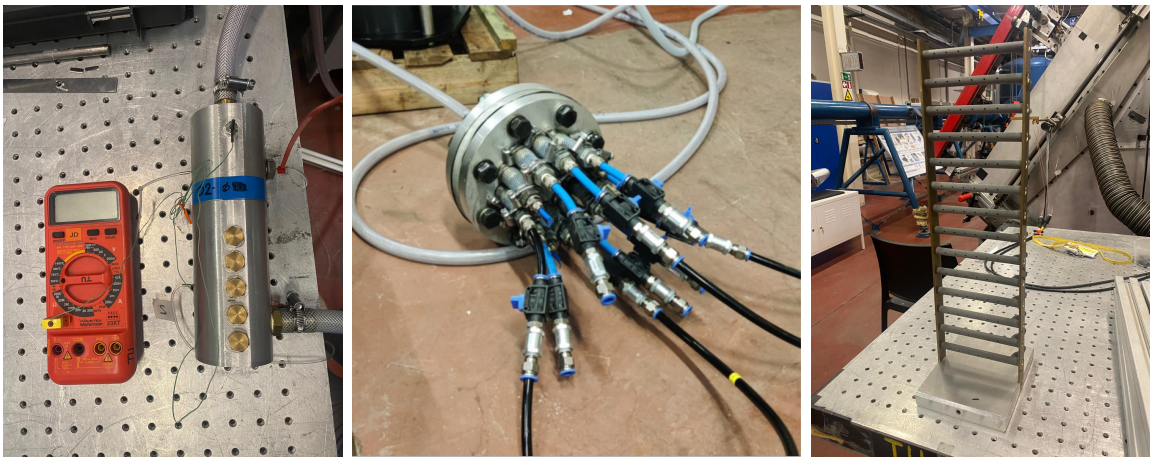

(a) (b) (c)

Figure 3.4: Active grid injection system. (a) Mass flow meter; (b) plenum; (c) turbulence grid.

3.4. Measurement systems

This section presents the measurement systems adopted in the experimental campaign. The instrumentation and procedures employed to ensure repeatable test conditions and to accurately characterize turbulence statistics are described. Three measurement stations are defined along the streamwise direction to characterize the inflow and outflow conditions and to provide a detailed description of the turbulence quantities. An overview of the operating principle of constant-temperature hot wire anemometry is also provided.

3.4.1. Instrumentation

For the experimental campaign the facility was equipped with multiple instrumentation stations providing access to the flow for the characterization of operating conditions, incoming turbulence and active-grid injection conditions. The measurement layout is organized into three stations along the streamwise direction. A schematization of the system is provided in Fig. 3.5, while real views of the test section are shown in Fig. 3.7 to facilitate a clearer understanding of the facility layout.

Station 0 (Facility inlet). Station 0 is located at half channel height immediately upstream of the turbulence grid, where the reference flow conditions were monitored. At this location, a Kiel probe was used to measure both total pressure, via a *Validyne* differential pressure transducer referenced to atmospheric pressure, and total temperature using an embedded thermocouple. These measurements were used to define the inlet

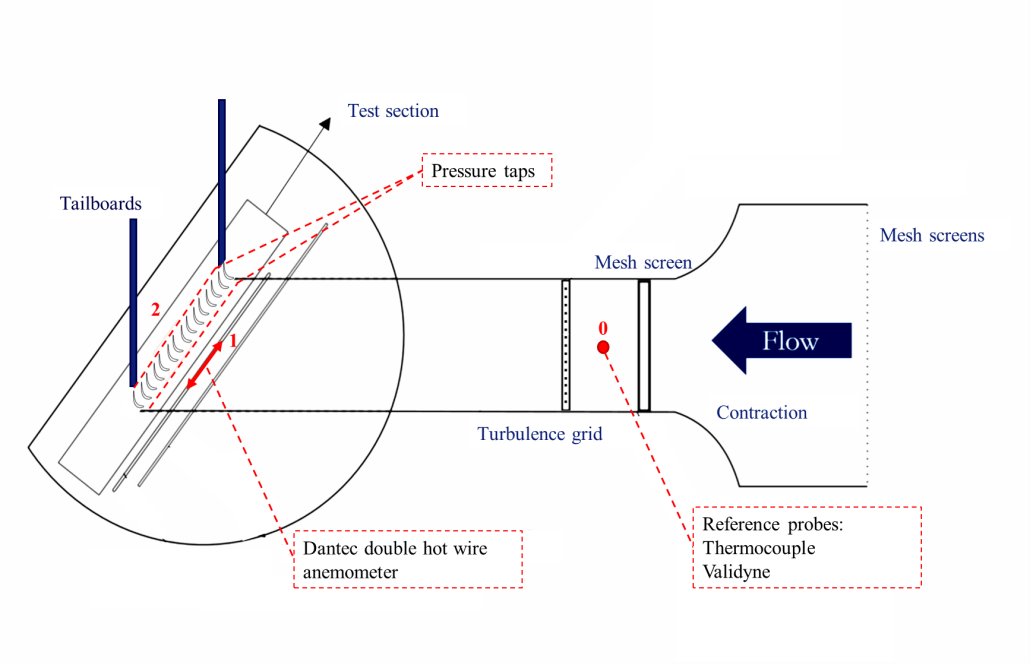

Figure 3.5: Schematization of instrumentation setup

conditions of the facility. Atmospheric pressure variations were continuously logged using a *Druck DPI 150* precision pressure indicator, allowing reconstruction of absolute total pressure from the differential measurements.

Station 1 (Cascade inlet). Station 1 is positioned upstream of the cascade. Turbulence measurements were performed using a *Dantec Dynamics* cross-wire hot wire probe (55P51), operated in constant temperature anemometry mode and connected to a *National Instruments USB-6251* data acquisition board with 16 analog inputs. The probe was traversed spanwise and pitchwise at a location half an axial chord upstream of the cascade leading edge. Accounting for the 55 mm length of the probe elbow arm, the effective measurement plane is located at a distance of approximately 1.4 axial chords upstream of the cascade. These measurements provided the incoming turbulence characteristics at the cascade inlet. During testing, the signal was sampled at 100 kHz for a sampling time of 20 s; the long acquisition time was selected to reduce the uncertainty associated with turbulence quantities.

During the initial phase of the experimental campaign, an alternative hot wire probe characterized by a different wire geometry was also tested at this measurement station. Preliminary measurements revealed a significant influence of probe geometry on the measured turbulence statistics, particularly affecting isotropy, as discussed in Appendix A. For this reason, this probe configuration was discarded and replaced by the *Dantec Dy-*

namics 55P51 cross-wire probe, which was adopted for all measurements presented in this thesis.

In addition, static pressure distributions along the endwalls were measured through pressure taps connected to a *Scanivalve MPS 4246-1 psi* transducer.

Station 2 (Cascade outlet). Station 2 is located downstream of the cascade. Endwall static pressure distributions were acquired through pressure taps connected to the *Scanivalve MPS 4246* system. These measurements were used to evaluate the static pressure at the outlet of the cascade. A needle five-hole pressure probe was also employed for the analysis of losses and wake characteristics downstream; however, since this lies outside the scope of the present thesis, those measurements were not considered.

(a) (b) (c)

Figure 3.6: Measurement systems. (a) Validyne membrane assembly; (b) hot wire probe; (c) Kiel reference probe.

Injected air measurement setup An additional measurement station was installed on the air injection system supplying the active turbulence grid, which operates independently of the main facility. The mass flow rate delivered to the grid was regulated through a critical nozzle. The upstream and downstream pressures across the nozzle were measured using *Validyne* differential pressure transducers, while the downstream temperature was measured using a digital multimeter (*Wavetek Meterman 23XT*) connected to a temperature sensor. These measurements were used to evaluate the pressure ratio across the nozzle and to verify choked-flow conditions. As discussed in Section 3.3, once choked operation was ensured, the injection mass flow rate, and therefore the injection

ratio (Eq. 3.2), could be determined. The injection ratio calculation routine was implemented in *LabVIEW* and displayed in real time on the control interface before testing. This allowed a simple verification that the desired injection ratio had been reached before the measurements were initiated.

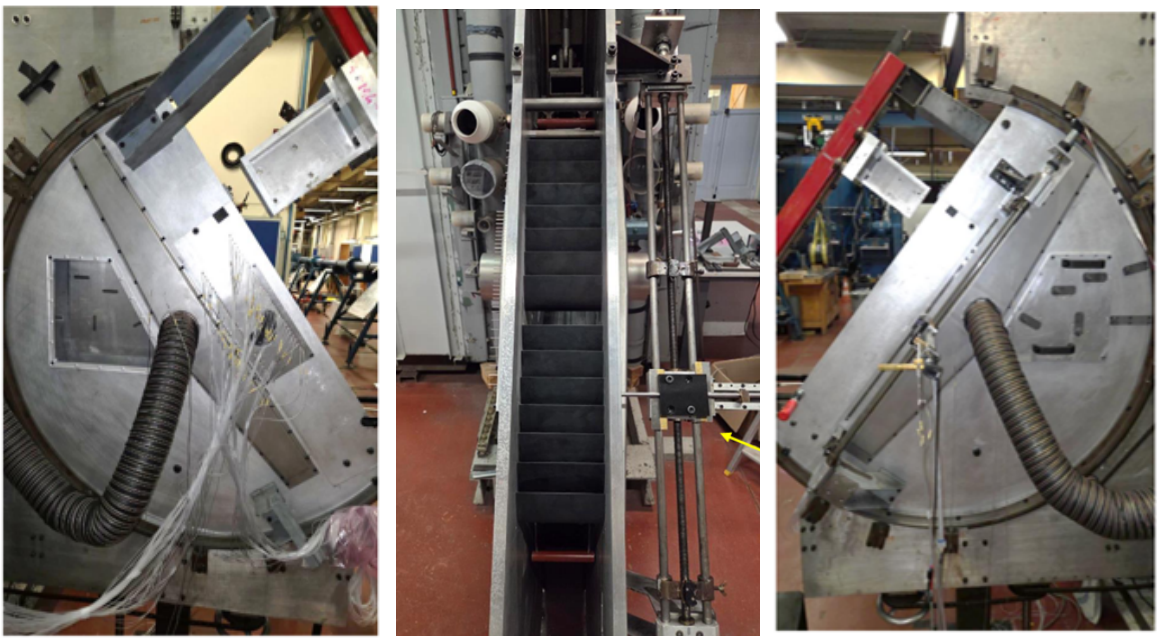

(a) (b) (c)

Figure 3.7: Side and front views of the test section. (a) Upstream and downstream pressure taps; (b) front view of the cascade; (c) hot wire upstream traversing system.

3.4.2. Hot wire anemometry

Hot wire anemometry (HWA) is one of the principal research tools for turbulence studies due to its ease-of-use, its high temporal resolution and its cost advantage compared to LDA (laser-Doppler anemometry) or PIV (particle-imaging velocimetry) systems. The operating principle of HWA relies on convective heat transfer from a thin electrically heated wire to the surrounding flow: as the flow velocity increases, the cooling rate of the wire increases, modifying its electrical resistance and thus the measurable voltage or current in the anemometer circuit.

Two main operational modes exist: in constant-current anemometry (CCA), the electrical current is kept constant and the wire temperature varies with flow velocity, resulting in a frequency response limited by the thermal inertia of the wire, while in constant-temperature anemometry (CTA) the wire resistance (and thus temperature) is kept constant through a feedback-controlled bridge circuit, providing improved temporal resolution

and making CTA the principal configuration adopted nowadays [7]. For this reason only CTA will be discussed in this section.

A complete hot wire measurement system is shown in Fig. 3.8 and consists of a probe with probe support and cabling, a CTA anemometer, a signal conditioner, an A/D Converter, and a Computer. The anemometer is controlled by *StreamWare Pro*, a software provided by *Dantec Dynamics* that allows digital configuration of the CTA and includes tools for velocity and angular calibration.

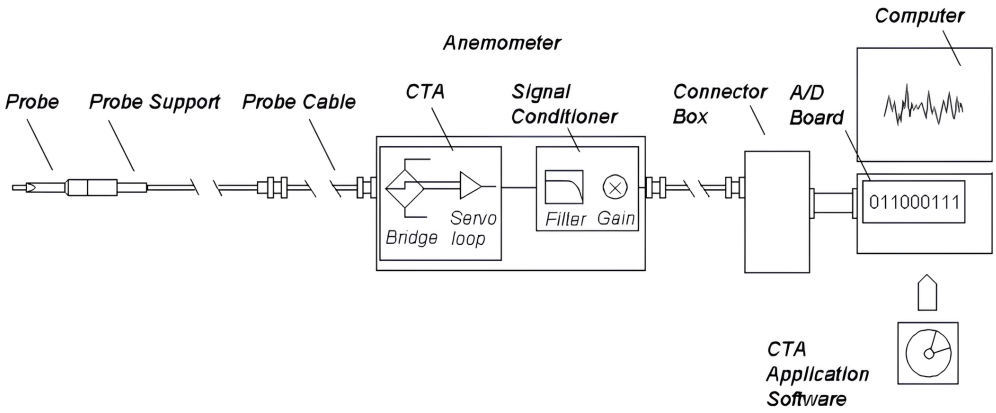

Figure 3.8: CTA measurement chain (from Jorgensen [14]).

In constant-temperature anemometry, the wire operating temperature T_w is maintained constant by imposing an *overheat ratio* a, defined as the relative increase of the wire resistance R_w at T_w with respect to its resistance at the ambient (reference) temperature R_{ref} [7, 14].

$$a = \frac{R_w - R_{ref}}{R_{ref}}$$

By setting the overheat ratio, the wire resistance is fixed and thus the wire temperature is defined and kept constant during testing. This is due to the relation between the electrical resistance and temperature expressed as

$$R_w = R_{ref}[1 + \alpha(T_w - T_{ref})] \tag{3.3}$$

where α is the temperature coefficient of resistance of the wire material. A commonly adopted material is platinum-plated tungsten ($\alpha \approx 0.0036\ ^\circ C^{-1}$).

In CTA operation, the wire forms one arm of a Wheatstone bridge (Fig. 3.9), which is

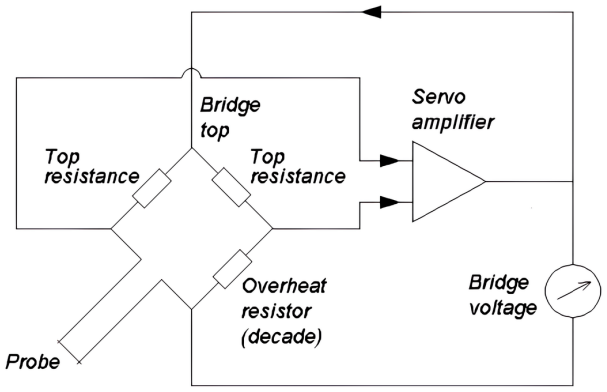

Figure 3.9: Constant temperature control circuit (from Jorgensen [14]).

continuously balanced through a high-gain feedback loop [14]. Any change in flow velocity affects the heat transfer with the wire, modifying its temperature and resistance. This resistance variation unbalances the bridge and generates an error signal that is amplified and used to adjust the electrical current supplied to the wire. The current is increased or decreased by the servo amplifier until the original resistance value is restored, ensuring that the wire temperature remains constant.

As a consequence, the bridge output voltage represents the electrical power required to maintain the wire at the imposed overheat temperature against convective cooling by the flow. Writing the steady-state energy balance for the heated wire leads to the formulation reported by Nagabushana and Stainback [23]:

$$E_b = R_{\text{tot}} \sqrt{\frac{\pi \, l \, k \, (T_w - \eta \, T_0) \; Nu}{R_w}}, \tag{3.4}$$

where l is the active wire length, k is the thermal conductivity of the fluid, T_w is the wire temperature, T_0 is the flow total temperature, Nu is the Nusselt number, and R_{tot} is the total electrical resistance of the circuit.

The factor η is the recovery temperature factor. In the vicinity of the wire, the fluid does not remain at the free-stream total temperature T_0 but is brought to a recovery temperature T_{adw} due to imperfect stagnation. The driving temperature difference for convective heat transfer is therefore $(T_w - T_{adw})$, which can be written as $(T_w - \eta T_0)$ by defining $\eta = T_{adw}/T_0$ [23]. In this work, the recovery factor was determined as $\eta = f(Re_w)$, where Re_w is the Reynolds number based on the wire diameter, from semi-empirical correlations proposed by Dewey [12].

The voltage measured by the anemometer E_b corresponds to the potential difference across the total circuit resistance, such that

$$R_{\text{tot}} = R_t + R_\ell + R_w,$$

where R_t is the bridge top resistance, R_ℓ is the lead resistance, and R_w is the wire resistance. More generally, the probe can be modeled as a chain of resistances (wire, prongs/support, cable, contacts), and variations in any of these elements modifies the calibration. This motivates minimizing reconnections and avoiding component replacement after calibration.

3.5. Determination of operating conditions

To ensure repeatable and comparable test conditions throughout the experimental campaign, the operating point of the cascade was defined and monitored using the exit isentropic Reynolds number at the cascade outlet (Station 2). The test were carried out at two operating conditions, namely $Re_{2,is} = 80,000$ and $160,000$.

The exit isentropic Reynolds number is defined as

$$Re_{2,is} = \frac{U_{2,is}\rho_2 C_{ax}}{\mu}$$

where μ is the the dynamic viscosity evaluated at the outlet conditions, and ρ_2 is the fluid density at Station 2. The isentropic velocity $U_{2,is}$ represents the velocity that the flow would reach at the cascade outlet if it expanded isentropically from the inlet total pressure P_{01} down to the static pressure P_2.

Generally, the inlet total pressure P_{01} is measured directly using a five-hole probe located upstream of the cascade. However, in the present experimental campaign this measurement was not available at Station 1. For this reason, P_{01} was reconstructed from hot wire measurements at Station 1 by combining the measured velocity with the local static pressure obtained from the pressure taps.
To make this reconstruction possible, some simplifying assumptions were introduced. Given the low-speed operation (inlet Mach number $M_1 \approx 0.03$), compressibility effects are negligible and the flow is assumed incompressible. Moreover, due to the lack of significant heat transfer, the total temperature is assumed constant and equal to the static temperature T_1:

$$T_{01} \approx T_{00} \approx T_1$$

Under these assumptions, the additional uncertainty introduced is expected to be small, and the dominant contribution to uncertainty remains associated with the hot wire measurement rather than density estimation or grid losses.

Assuming incompressible flow, the inlet total pressure can be obtained from the Bernoulli relation evaluated at Station 1:

$$P_{01} = P_1 + \frac{1}{2}\rho_1 U_1^2 \tag{3.5}$$

where P_1 is the static pressure measured by the upstream pressure taps and U_1 is the velocity obtained from the hot wire calibration. Under the incompressibility assumption, the density at Station 1 is estimated using the reference probe measurements at Station 0 as

$$\rho_1 \approx \frac{P_1}{RT_1} \tag{3.6}$$

Once the inlet total pressure P_{01} has been reconstructed, the isentropic Mach number at the cascade outlet, and consequently the isentropic exit velocity $U_{2,is}$ can be derived from the pressure ratio P_2/P_{01}, where P_2 is the static pressure measured by the downstream pressure taps at Station 2.

This procedure was implemented in the LabVIEW control routine to monitor the exit isentropic Reynolds number in real time and to ensure that the desired operating conditions were reached and maintained throughout the measurements.

3.6. Data acquisition and processing

3.6.1. Hot wire calibration

The calibration procedure of the hot wire adopted in this work was performed ex situ using a *Dantec StreamLine Pro* Automatic Calibrator, which provides a well-controlled and repeatable reference flow for hot wire calibration. The procedure is divided into two main steps. The first step focuses on the determination of the effective wire temperature and establishes a nondimensional velocity calibration, which is common to both single- and multi-wire probes. The second step addresses the angular sensitivity of the probe and is required only for multi-wire configurations, where the response of each wire depends on its orientation relative to the flow. These two aspects are treated separately in the following subsections.

Wire temperature determination

As highlighted by Eq. 3.4, the bridge voltage depends on several flow and probe parameters. In its most general form, this dependency can be expressed as

$$E_b = f(wire\ geometry, \rho, T_0, \mathbf{U}, \alpha, \beta)$$

where α and β are the yaw and pitch angles between the probe and the incoming flow. The most common calibration approach, known as King's law [15], relates E_b directly to the flow velocity U through the empirical relation

$$E_b^2 = a + bU^n$$

where b and n are calibration constants determined by systematically varying the velocity, and $a = E_{b,0}^2$ represents the bridge offset at zero velocity. This formulation, however, is strictly valid only for isothermal, incompressible flows with the incoming flow perpendicular to the wire. In more realistic conditions, the calibration is strongly sensitive to variations in velocity, density, and total temperature.

When calibration is performed under fixed thermodynamic conditions (e.g., ambient pressure) for a given probe, E_b effectively depends on both flow velocity and total temperature. As a result, variations in total temperature cause a shift of the dimensional calibration curve $E_b - U$ as shown in Fig. 3.10a. For non isothermal flows, a non dimensional calibration procedure is preferred.
In this approach, calibration is expressed in terms of the Nusselt number, computed from E_b using Eq. 3.4 [9]. A non-dimensional analysis in terms of Nu is advantageous because, since

$$Nu \propto \frac{E_b^2}{T_w - \eta T_0}$$

it incorporates the temperature difference driving heat transfer. As a result, the explicit temperature dependence present in the dimensional E_b–U calibration is removed. The Nusselt number formulation collapses data obtained at different total temperatures onto a single curve.
For incompressible continuum flows, the Nusselt number depends uniquely on the wire Reynolds number and the flow direction:

$$Nu = f(Re_w, \alpha, \beta)$$

In the present first calibration step, the probe is maintained in a fixed reference orientation aligned with the mean flow. Directional effects are therefore neglected, allowing

construction of a unique $Nu - Re_w$ relationship. This method effectively removes the temperature dependence in dimensional $E_b - U$ calibration curves (Fig. 3.10b).

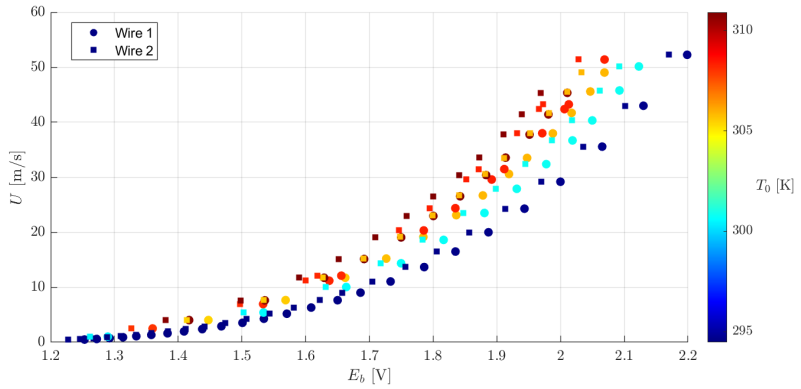

(a)

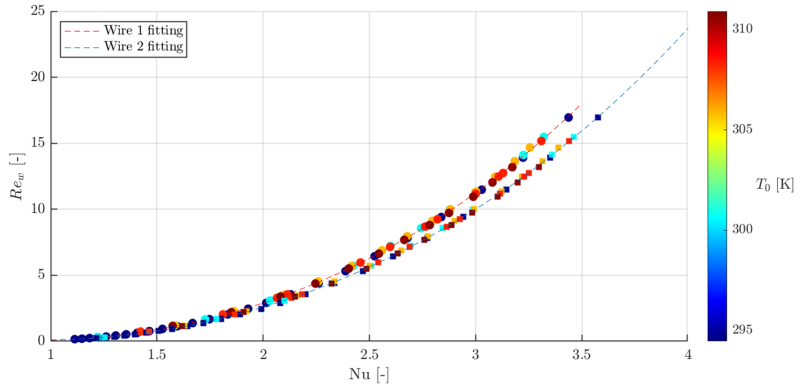

(b)

Figure 3.10: Dantec cross wire 55P51 calibration curves. (a) Bridge voltage E_b recorded by both wires vs flow velocity for different total temperatures T_0; (b) Corresponding nondimensional calibration in terms of $Nu - Re_w$, dashed lines represent fourth-order polynomial fits.

It is to be noted that the effective wire temperature T_w in Eq. 3.4 is not known a priori: T_w is not perfectly uniform along the wire length, thus it generally differs from the value imposed by the overheat ratio.
Following the methodology of Cukurel et al. [9], the effective wire temperature is determined iteratively. Candidate values of T_w are assumed, the corresponding Nu values are recomputed, and the value of T_w that provides the best collapse of the $Nu - Re_w$ calibration data obtained at different flow temperatures (for example by maximizing the coefficient of determination R^2) is selected.

To determine the effective wire temperature using this approach, a calibration was performed, where the flow velocity and total temperature were systematically varied over the

ranges approximately 0–50 m/s and 20–40 °C, respectively (Fig. 3.10a).
Once the $Nu - Re_w$ curve has been established, calibration becomes independent of the flow temperature. For a given measurement, the wire Reynolds number Re_w can be obtained from the measured voltage through the curve and the flow velocity can then be recovered provided the fluid density ρ is known. This calibration procedure, therefore, requires independent measurements of pressure and temperature in order to decouple the velocity from the Reynolds number.

Angular calibration

In multi-component hot wire measurements, the wire response depends not only on the magnitude of the flow velocity but also on the direction of the incoming flow relative to the wire. When a wire is inclined with respect to the flow, the component of velocity normal to each wire changes, which modifies the convective heat transfer and therefore the measured bridge voltage. This effect introduces an angular sensitivity that must be characterized through an angular calibration to be performed once the $Nu - Re_w$ relationship has been established at a reference probe orientation.
The calibration is carried out in the *Dantec* calibrator by yawing the probe over a prescribed angular range while maintaining controlled velocity and total temperature conditions. During this procedure, the probe is rotated with respect to the mean flow direction, and the bridge voltages of the individual wires are recorded.
Instead of constructing a fully multidimensional calibration in terms of (U, T_0, α, β), the methodology proposed by Cukurel et al. [9] introduces the concept of an *effective Reynolds number*. For a given yaw angle, the measured voltage is first converted into a Nusselt number and then projected onto the previously determined $Nu - Re_w$ calibration curve. The Reynolds number obtained in this manner, denoted Re_{eff}, corresponds to the value that would produce the same heat transfer if the wire were aligned with the reference flow direction. The angular response of each wire can therefore be expressed in nondimensional form as

$$\frac{Re_{eff,i}(\alpha)}{Re_w} = f(\alpha) \tag{3.7}$$

which experimentally collapses onto a single curve independent of Reynolds number and Mach number [9]. For a cross-wire probe, two such relations are obtained, one for each wire as shown in Fig 3.11a.

The instantaneous yaw angle is then determined from the ratio of the effective Reynolds numbers of the two wires, which eliminates the explicit dependence on the actual Reynolds

number Re_w (Fig. 3.11b).

$$\alpha = f\left(\frac{Re_{eff,1}}{Re_{eff,2}}\right) \tag{3.8}$$

In this manner, the angular calibration is fully decoupled from temperature and compressibility effects, and only two non dimensional curves, the $Nu - Re_w$ relation and the angular response function, are required to determine both flow velocity and direction.
An estimate of the measurement uncertainty for the calibration curves $Re = f(Nu)$ and $\alpha = f(Re_1/Re_2)$ is given in Table 4.3.

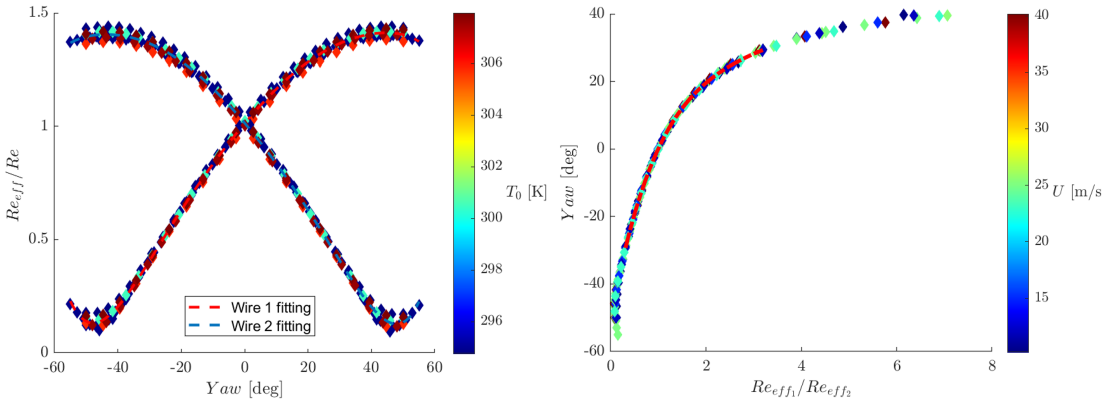

(a) (b)

Figure 3.11: Dantec cross wire 55P51 directional sensitivity.(a) Individual angular response of each wire; (b) Angular calibration curve. The red dashed line represents the fourth-order polynomial fit performed over the range where the measurements show the best collapse.

3.6.2. HWA post-processing methodology

The post-processing methodology adopted for the HW probe follows:

- The bridge voltages of the two wires, $E_{b1}(t)$ and $E_{b2}(t)$, were digitally filtered using a zero-phase Butterworth low-pass filter with cutoff frequency $f_c = 30$ kHz.
- The local thermodynamic state of the flow was prescribed using the reference instrumentation. The total temperature T_0 was obtained from thermocouple measurements, while the local density ρ was retrieved from Eq. 3.6. The dynamic viscosity μ was evaluated from Sutherland's law [30].
- Equation 3.4 was applied to compute the instantaneous Nusselt numbers of the two wires, $Nu_1(t)$ and $Nu_2(t)$, from the bridge voltages and the wire geometrical and electrical properties.

- The instantaneous effective Reynolds numbers were obtained from the non-dimensional calibration curves (Fig. 3.10b), namely

$$Re_{w1,\text{eff}}(t) = f_1(Nu_1(t))\,, \qquad Re_{w2,\text{eff}}(t) = f_2(Nu_2(t))\,,$$

- Using the angular calibration curve of Eq. 3.8, the ratio $Re_{w1,\text{eff}}(t)/Re_{w2,\text{eff}}(t)$ was converted into the instantaneous yaw angle $\alpha(t)$.

- The Reynolds number magnitude was reconstructed using the angular sensitivity functions (Fig. 3.11a):

$$Re(t) = \frac{Re_{wi,\text{eff}}(t)}{f_i(\alpha(t))}, \qquad i = 1, 2,$$

  from which the instantaneous velocity magnitude was obtained as

$$U(t) = \frac{Re(t)\,\mu}{\rho\, d_w}.$$

- The instantaneous in-plane velocity components in the probe frame of reference were obtained by trigonometric projection:

$$u_x(t) = U(t)\cos\alpha(t), \qquad u_y(t) = U(t)\sin\alpha(t).$$

- Velocity fluctuations were obtained through Reynolds decomposition and the turbulence intensity was then computed by combining the two measured in-plane components in a form which represents the two-component equivalent of Eq. 2.5.

$$Tu = \frac{\sqrt{\frac{1}{2}\left(u_{\text{rms}}^2 + v_{\text{rms}}^2\right)}}{\overline{U}} \times 100,$$

- The turbulence isotropy in the measured plane was quantified using the ratio of normal stresses:

$$Iso = \left(\frac{u_{\text{rms}}}{v_{\text{rms}}}\right)^2.$$

  Values close to unity indicate near-isotropic turbulence in the two orthogonal directions. Locations where Iso exceeded a prescribed threshold were flagged as non-isotropic for subsequent analysis.

4| Proposed method for length scale estimation

This chapter presents the methodology developed in this work for estimating the longitudinal integral length scale based on steady hot wire measurements acquired upstream of the cascade (Station 1 in Fig. 3.5). The objective is to define a consistent and reproducible procedure that overcomes the limitations of classical approaches, as will be further discussed in Section 4.1.
It is important to note that this chapter does not aim to provide a general or purely theoretical discussion of alternative methodologies. Instead, the focus is on illustrating concretely how the proposed method is implemented and applied to a specific reference test case. The reference case is used as an example to demonstrate the workflow, parameter selection, convergence criteria, and uncertainty assessment associated with the procedure. Through this example, the robustness and consistency of the methodology are assessed before extending the analysis to additional experimental configurations in the following chapter.

The chapter is structured as follows. Section 4.1 discusses the limitations of classical definitions and motivates the need for a model-based iterative approach. Section 4.2 introduces the conceptual framework of the proposed method and describes the fitting strategy, including the selection of model parameters. Section 4.3 addresses the uncertainty analysis, distinguishing between statistical and measurement contributions. Together, these sections define a complete and reproducible procedure for integral length scale estimation, which is first validated on the reference test case and subsequently applied to additional experimental configurations to assess its general applicability.

4.1. Limitations of classical definitions

While the integral length scale is classically defined through integration of the autocorrelation coefficient $\rho(\tau)$ (Eq. 2.9), its practical estimation from experimental data presents several challenges. The formal definition requires integration over an infinite time duration, but in practice the autocorrelation function can only be computed from finite measurements, raising immediate questions about the appropriate integration limits.

At larger lags, the behavior of the autocorrelation function is particularly problematic. Ideally, $\rho(\tau)$ should decay monotonically to zero for higher lags, but in experiments $\rho(\tau)$ exhibits an oscillatory tail which persists for many multiples of the integral time scale. Yaglom [37] demonstrated that, for finite datasets, such oscillations are often dominated by statistical errors rather than physical correlations and should therefore be regarded as spurious. Including these regions in the integration can lead to biased estimates of the integral time scale.

As previously mentioned in Section 2.3, a common practical approach consists in truncating the integration at the first zero-crossing of the autocorrelation function, thus excluding the large lag region where convergence is poorest. O'Neill et al. [24] showed that this criterion generally provides more robust estimates than integrating over the entire available domain, provided that the measurement window is sufficiently long. Nevertheless, the first zero-crossing is not always well defined in experimental data. In hot wire measurements, limited acquisition times and low frequency leakage may result in autocorrelation functions that either do not cross zero [22] or exhibit large variability in the location of the first zero. Such test-to-test variability was observed in the present experimental campaign, with both the zero-crossing location and the resulting length-scale estimates varying between nominally identical tests performed on the same day (Fig. 4.1).

Lewalle and Ashpis [18] argued that equivalent integral scales can be obtained more robustly from the low frequency limit of the energy spectrum, where convergence properties are superior to those of the autocorrelation tail. Taken together, these considerations motivate a shift away from autocorrelation based methods toward spectral based approaches. Due to the equivalence between the autocorrelation function and the spectrum, the integral length scale can then be expressed using Eq. 2.33 in terms of the zero-frequency limit of the spectrum. The practical implications of this reformulation are illustrated in Table 4.1, which reports integral length scale estimates obtained from two independent acquisitions using both autocorrelation based and spectral based methods. The reported data highlight significantly reduced test-to-test variability of the spectral approach showing improved robustness.

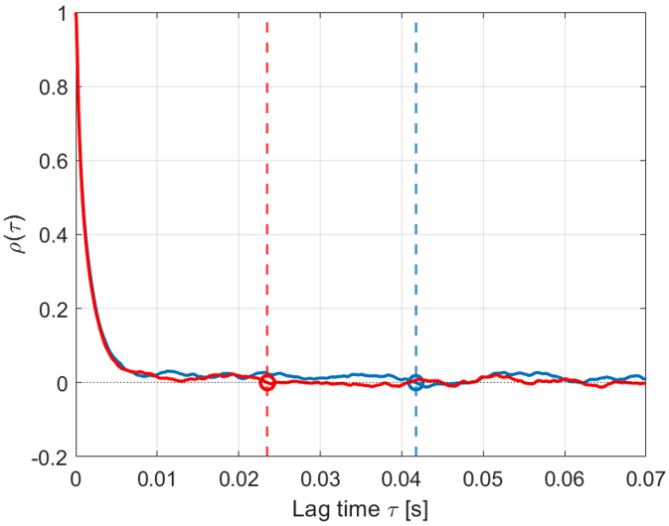

Table 4.1: Integral length scale estimates

Description	**Value**
Autocorrelation approach	
Test 1 [mm]	17.3
Test 2 [mm]	21.8
Relative difference	20%
Spectral approach	
Test 1 [mm]	13.4
Test 2 [mm]	12.9
Relative difference	4%

Figure 4.1: Autocorrelation coefficient $\rho(\tau)$ and corresponding integral length scale estimates obtained from two independent acquisitions performed under identical flow conditions. The dashed lines mark the first zero-crossing of each $\rho(\tau)$.

However, spectral methods do not entirely eliminate convergence issues, but instead transfer them to the estimation of the low frequency plateau. In experimental data, the zero-frequency limit must be extrapolated by averaging the spectrum over an arbitrary low frequency range, making the resulting integral scale dependent on the choice of this averaging interval [3]. Moreover, plain averaging in the low frequency region is ineffective, as this part of the spectrum is highly susceptible to fluctuations and inaccuracies. Such variability can introduce bias into the extrapolation, particularly for finite signal lengths [18]. As a result, although this spectral approach exhibits more stable and consistent length scales results compared to autocorrelation based methods, it remains difficult to assess the reliability of a given estimate, which is tied to assumptions made in the zero-frequency extrapolation procedure.

Figure 4.2a illustrates how the estimated integral length scale varies as the averaging bandwidth is progressively extended toward the end of the energy-containing range (i.e., the flat portion of the spectrum). No clear plateau or stabilization region emerges that would allow an objective selection of an optimal upper frequency limit f_{max} within this range. Consequently, the choice of a specific averaging interval appears essentially arbitrary. The variability induced solely by the choice of f_{max}, considering the sensitivity band of the Λ_x values shown in Fig. 4.2a ($p5 - p95 = 13.8 - 16.5$mm), amounts to approximately ± 1.3 mm, compared to the much smaller ± 0.3 mm obtained with the proposed method, as will be shown in Section 4.2.4.

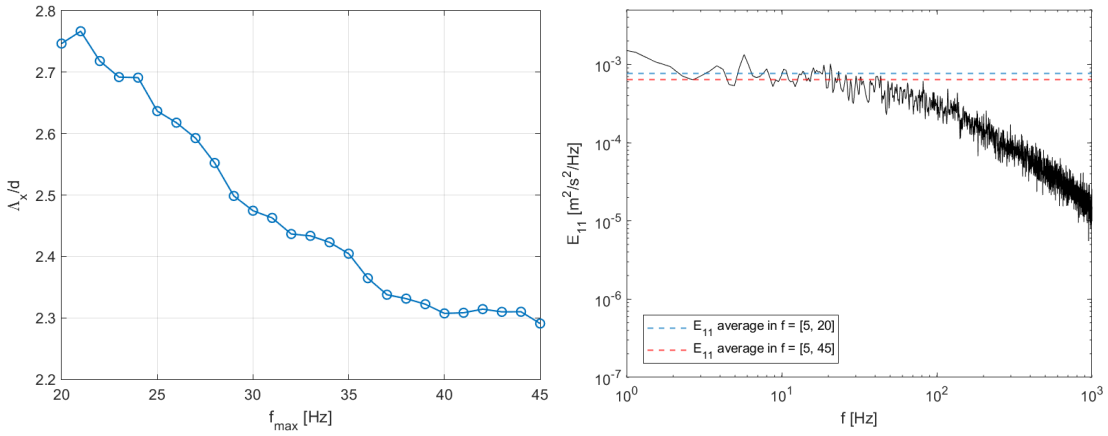

(a) (b)

Figure 4.2: (a) Λ_x/d ($d = 6$ mm, grid bar diameter) vs upper frequency limit f_{max} used in the low frequency spectral averaging procedure. (b) Experimental spectrum with two averaging intervals.

In light of this sensitivity, the fundamental question remains: which value of f_{max} should be selected? Without a physically grounded or statistically robust selection criterion, any single choice remains subjective.

These limitations motivate the development of a spectral based method for estimating the integral scale that avoids low frequency averaging and reduces sensitivity to subjective parameter choices, while retaining the improved stability.

4.2. Conceptual framework of the proposed method

To avoid the use of arbitrary inputs and to establish a consistent spectral method for estimating the integral length scale, an automated optimization-based approach is adopted. The central idea is to determine the length scale by minimizing the difference between the experimental energy spectrum and a theoretical spectrum model. In this framework, the integral length scale is treated as an unknown parameter and identified through a bounded one-dimensional minimization procedure. The overall logic of the method is schematically illustrated in Fig. 4.3.

4.2.1. Definition of the objective function

Two theoretical models are considered in this study: the von Kármán spectrum (Eq. 2.29) and the Pope spectrum model (Eq. 2.26). Both are formulated as three-dimensional spectra and transformed into their one-dimensional forms through the isotropic relation

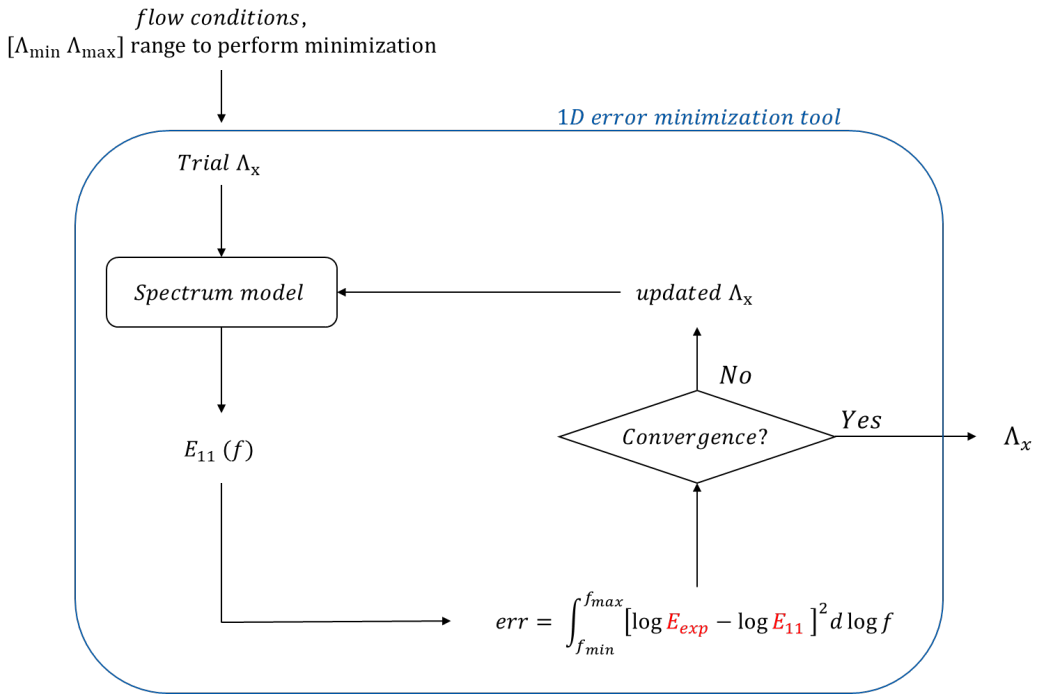

Figure 4.3: Conceptual block diagram of the proposed longitudinal length scale estimation method.

(Eq. 2.21). To enable direct comparison with hot wire measurements, the spectra are expressed in the frequency domain via Taylor's frozen turbulence hypothesis (Eq. 2.23). Since the theoretical spectral models considered are derived under the assumption of homogeneous isotropic turbulence, the proposed method is applicable only when this assumption is reasonably satisfied. In practice, this corresponds to isotropic grid-generated turbulence at sufficiently high Reynolds numbers, where Kolmogorov's similarity hypothesis holds and a well defined energy cascade is present.

The discrepancy between experimental and theoretical spectra is quantified through an objective function formulated as a logarithmic least-squares error integrated with respect to $d(logf)$ over the interval $[f_{min}, f_{max}]$. The selection of this frequency range will be discussed in depth in Section 4.2.4.
Integrating with respect to $d(logf)$ rather than df implies that each frequency decade contributes equally to the objective function. As a result, the fitting procedure does not overweight high frequency regions, even though the spectrum contains a larger number of discrete sample points at higher frequencies. This aspect is particularly important because the primary objective of the method is to accurately reproduce the low frequency portion of the spectrum, which governs the large energy-containing scales and directly determines the value of the integral length scale.

4.2.2. Spectral estimation and smoothing effect

The experimental Power Spectral Density (PSD) is computed from the measured longitudinal velocity fluctuations using the MATLAB *pwelch* function, which implements Welch's averaged periodogram method [36]. This method estimates the spectrum by dividing the signal into overlapping segments, computing modified periodograms for each segment, and averaging them. The averaging process reduces the variance of the spectral estimate, resulting in a smoother spectrum, although at the expense of reduced frequency resolution. A smooth spectral shape is particularly important for the fitting procedure, as it significantly improves the robustness and stability of the minimization. Compared to arbitrary post-processing smoothing techniques, the use of *pwelch* provides a statistically consistent and reproducible approach.

In *pwelch*, the length of the segments into which the signal is divided is specified as an integer input that defines both the length of each segment and the length of the applied Hamming window. Dividing and averaging the signal with shorter segments increase the degree of averaging and thus produce a smoother spectrum, but they also reduce frequency resolution, particularly at low frequencies as can be seen in the bottom panel of Fig. 4.4. In the present work, for acquisitions at 100 kHz and 20 seconds duration, a Hamming window of 200000 samples is selected as a compromise between variance reduction and frequency resolution. Figure 4.4 reports both the effect of window selection

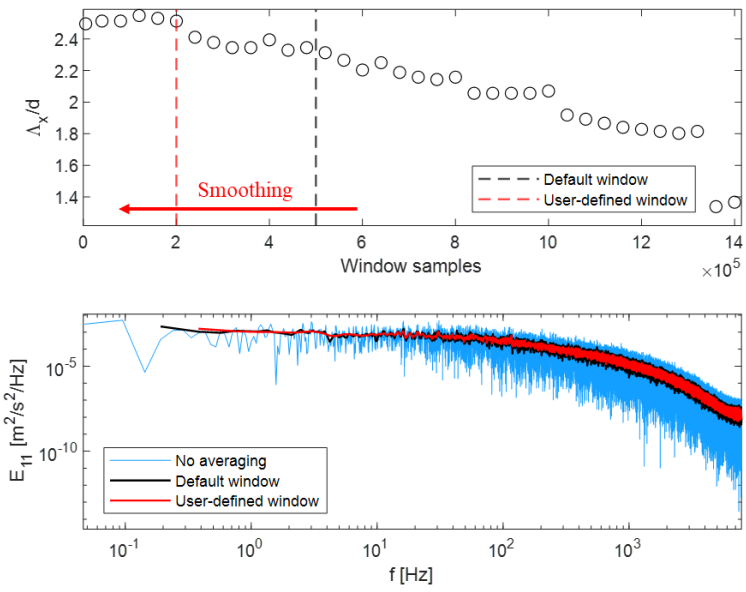

Figure 4.4: Top: Effect of window selection on Λ_x/d (d = 6 mm, grid bar diameter) computed through the von Kármán fitting. Bottom: corresponding power spectra.

on the estimated Λ_x and the corresponding power spectra. As the number of samples per window decreases, the variance reduction improves the stability of the fitting procedure and the integral length scale estimate progressively converges toward a stable value, as shown in the upper panel of the figure. The smoother spectral shape therefore results in an increasingly accurate length scale estimation. These considerations must be adapted for signals of different durations, since the appropriate window length depends on the total number of samples.

A comparison between the adopted window length and MATLAB's default *pwelch* settings shows a difference in the final Λ_x value of approximately 1.12 mm. The corresponding relative variation, computed as the ratio between this difference and the mean estimated value, is about 7.8%.

4.2.3. Numerical minimization strategy

In this study, the error minimization of the objective function is performed with the MATLAB tool *fminbnd*, which is a one-dimensional minimizer of a real-valued, scalar function of a single variable within a specified finite interval of possible Λ_x values [a,b]. The function *fminbnd* finds a point $x* \in [a, b]$ such that

$$f(x*) \leq f(x) \forall x \in [a, b]$$

subject to the assumption that the function is continuous on the interval.

The convergence of *fminbnd* is determined by the size of the interval. The algorithm progressively shrinks the search interval that is guaranteed to contain the minimum until a tolerance $TolX$ on the interval size is met. $TolX$ is set to the MATLAB default 10^{-4}.

$$|b - a| < TolX$$

Since *fminbnd* is a local minimization algorithm, if multiple local minima exist within the interval $[a, b]$, the method will converge to only one of them. The specific minimum obtained depends on the function's shape and the sequence of trial points generated during the search. Consequently, the solution returned by *fminbnd* is not guaranteed to correspond to the global minimum over the interval. To address this limitation, a grid search procedure was also implemented, in which the objective function is evaluated for a large number of uniformly spaced Λ_x values across $[a, b]$. The Λ_x that yields the minimum value of the objective function can be considered an approximation of the global minimum, with an accuracy that depends on the chosen grid resolution.

The results of the grid search were found to be in agreement with those obtained using *fminbnd*, supporting the validity of the *fminbnd* solution. Given its significantly lower computational cost compared to exhaustive grid sampling, *fminbnd* was therefore adopted for the analysis.

Although the iterative framework establishes an objective procedure for estimating the integral length scale, its implementation requires the definition of certain fitting parameters. In particular, the frequency interval $[f_{min}, f_{max}]$ must be specified, and adequate low frequency convergence of the experimental spectrum must be ensured. These inputs are not prescribed arbitrarily; rather, their selection is guided by sensitivity analyses. Figure 4.5 highlights the fitting limits within which a fitting of the experimental data is performed with the Von Kármán spectrum formulation. The procedure adopted for determining appropriate fitting parameters and the influence of signal duration on the results are presented in the following subsections.

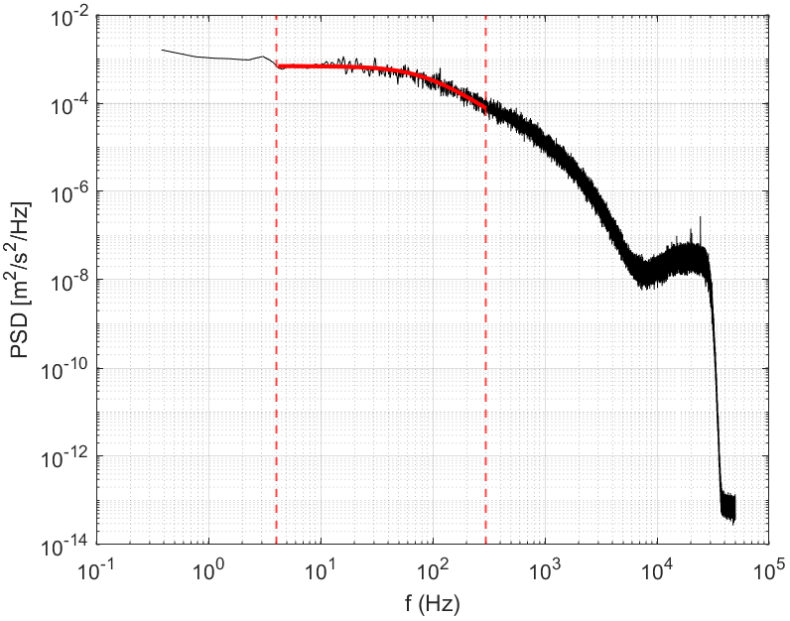

Figure 4.5: Power spectral density of the measured longitudinal velocity fluctuations (black) and fitted von Kármán spectrum (red). The vertical dashed lines indicate the lower and upper fitting limits f_{min} and f_{max} used in the fitting procedure.

4.2.4. Selection of fitting parameters

Before analyzing the individual effects of f_{min} and f_{max} it is important to underline that the integral length scale depends simultaneously on both fitting limits. This means that the curves shown in the following figures represent only partial projections of a two-dimensional dependency. For instance, the sensitivity of Λ_x to f_{max} is not unique, as

different values of f_{min} would generate slightly different curves, and vice versa.

In this section, the behavior associated with each fitting limit is first examined separately in order to isolate and describe each effect. A comprehensive two-dimensional sensitivity map will then be presented at the end of the chapter to synthesize these effects and identify the optimal fitting domain.

Upper limit

When selecting the upper fitting limit f_{max}, it is important to take into account that the integral length scale is primarily determined by the energy-containing range at low frequencies; therefore, the fitting procedure should prioritize a good representation of this portion of the spectrum. Increasing f_{max} progressively incorporates larger portions of the high frequency spectrum into the fitting procedure. As a result, deviations between the experimental spectrum and theory at high frequencies may bias the optimization and deteriorate the quality of the fit in the energy-containing region. On the other hand, if f_{max} is chosen too small, the fitting interval becomes narrow and the minimization may become sensitive to isolated spectral peaks or valleys arising from statistical variability of the PSD estimate.

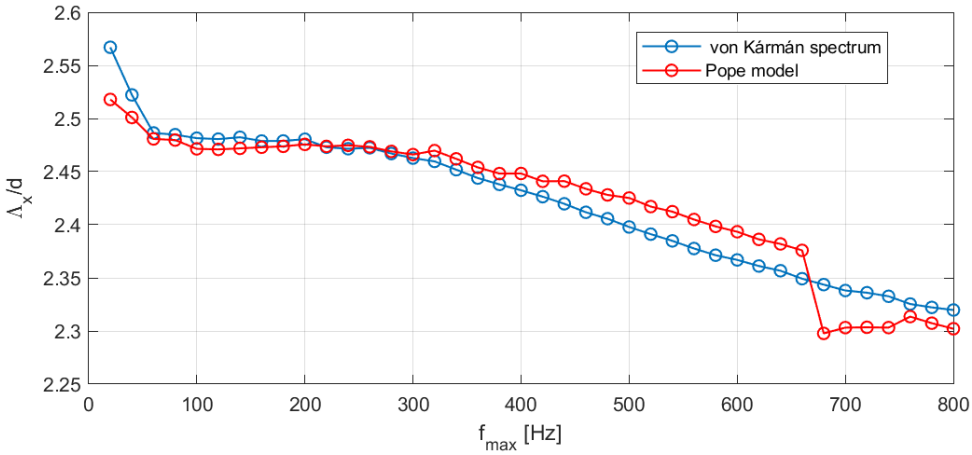

Figure 4.6: Sensitivity of the estimated integral length scale Λ_x/d (d = 6 mm, grid diameter) to the upper fitting limit f_{max} for the von Kármán and Pope spectral models

This behavior is illustrated in Fig. 4.6 which shows the sensitivity of the estimated integral length scale Λ_x to the upper fitting limit f_{max} for both the von Kármán and Pope spectral models. An intermediate range, approximately between 100 and 300 Hz, can be identified in which Λ_x remains nearly constant. This stabilization indicates the existence of a balanced fitting interval in which the energy-containing range is sufficiently represented

while the influence of higher frequency discrepancies remains moderate.

As discussed in Section 2.5.1, the two theoretical spectra differ in their ranges of validity. The von Kármán formulation represents only the energy-containing and inertial subranges, whereas the Pope model extends into the dissipation range.
From graphical considerations of the measured spectrum, the inertial subrange, identified by the $-5/3$ slope, extends approximately up to 800 Hz. Beyond this frequency, the spectrum progressively deviates from the inertial scaling and transitions into the dissipation range. Since, as previously mentioned, the objective of the present procedure is to fit the energy-containing region that is modeled by both formulations, the fitting interval must be restricted to the range in which both models are physically valid, i.e. $f_{max} \leq 800$ Hz as showed in Fig. 4.6.

Notably, both spectral models exhibit nearly identical trends over the entire range of f_{max}, with the curves closely overlapping in Fig. 4.6. This consistency indicates that the observed sensitivity is not model specific but rather intrinsic to the fitting procedure.

Lower limit

The selection of the lower limit of the fitting interval, f_{min}, requires particular attention, as the fitting procedure is especially sensitive to this parameter. In practice, variations in f_{min} lead to larger changes in Λ_x than comparable variations in f_{max}. This behavior reflects the reduced stability and convergence of the lowest frequency portion of the spectrum.

For f_{min} to be appropriate, the estimated length scale should remain stable when f_{min} is varied within a reasonable range in the energy-containing region. Such stabilization indicates that the spectrum has reached a sufficiently flat behavior at low frequencies and that the largest energy-containing scales are adequately resolved. Achieving this condition requires sufficient frequency resolution, which in practice implies longer signal acquisition times. The influence of signal duration on spectral convergence will be discussed in detail in the following section; here, only the trend of Λ_x as a function of f_{min}, for a fixed signal duration of 20 seconds, is presented in Fig. 4.7.

For very small values of f_{min} (1–2 Hz), larger values of Λ_x are obtained due to spectral leakage. In this range, the spectrum exhibits an artificial rise, indicating an apparent increase in energy that is not physically representative of the turbulent flow. This excess low frequency energy is primarily attributed to non-stationary effects, such as slow variations of the mean velocity occurring over time scales comparable to or longer than the acquisition window.

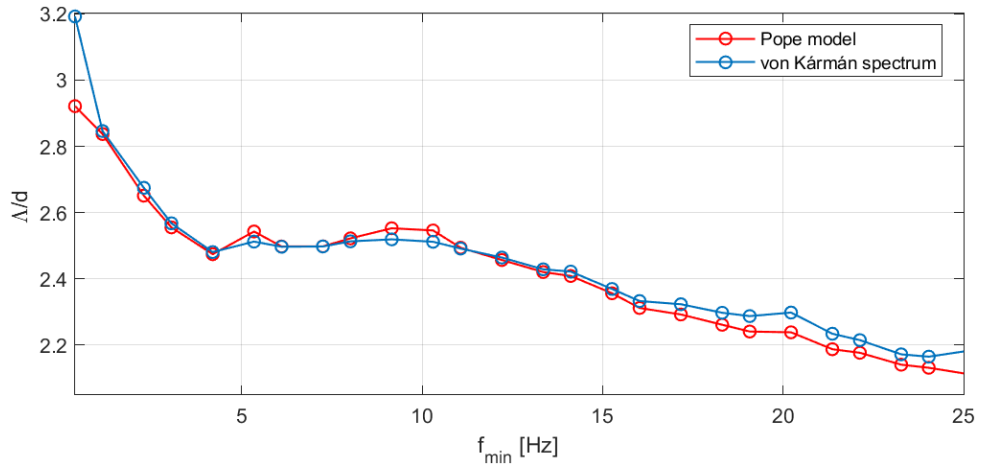

Figure 4.7: Sensitivity of the estimated integral length scale Λ_x to the lower fitting limit f_{min} for a 20 seconds record, comparing von Kármán and Pope spectral models

In fact, repeated measurements performed at the same spatial location and at the same test conditions yield spectra that differ only in this lowest frequency region, while the rest of the spectrum remains essentially unchanged (see Fig. 5.6). This behavior confirms that the observed trend at low frequencies is test-dependent and does not reflect turbulence dynamics.

The proper selection of f_{min}, taken within the flat region of the spectrum, helps to remove the problematic low frequency components that ultimately disturb the autocorrelation function, particularly its zero-crossing location, as discussed in Section 4.1.
If leakage effects are visible in the first frequency bins (for example, around 2 Hz in Fig. 4.7), the fitting interval can be intentionally shifted to slightly higher frequencies, such as 3-4 Hz, to exclude the affected portion of the spectrum. In practice, f_{min} may even be chosen more conservatively (e.g., 6-7 Hz) to ensure that only the flat and well-converged region of the spectrum is included in the minimization. By doing so, variability induced by leakage is avoided.
Beyond the stabilization region of Λ_x, approximately 4–12 Hz, the estimated length scale begins to decrease as f_{min} increases. This behavior is expected, since progressively higher values of f_{min} exclude physically relevant low frequency content from the fitting interval. As a result, the energy-containing range becomes too narrow to obtain a reliable measure of the largest scales.

Combined limits

Figure 4.8 summarizes the combined influence of the lower and upper fitting limits on the estimated integral length scale. Three distinct regions can be identified.

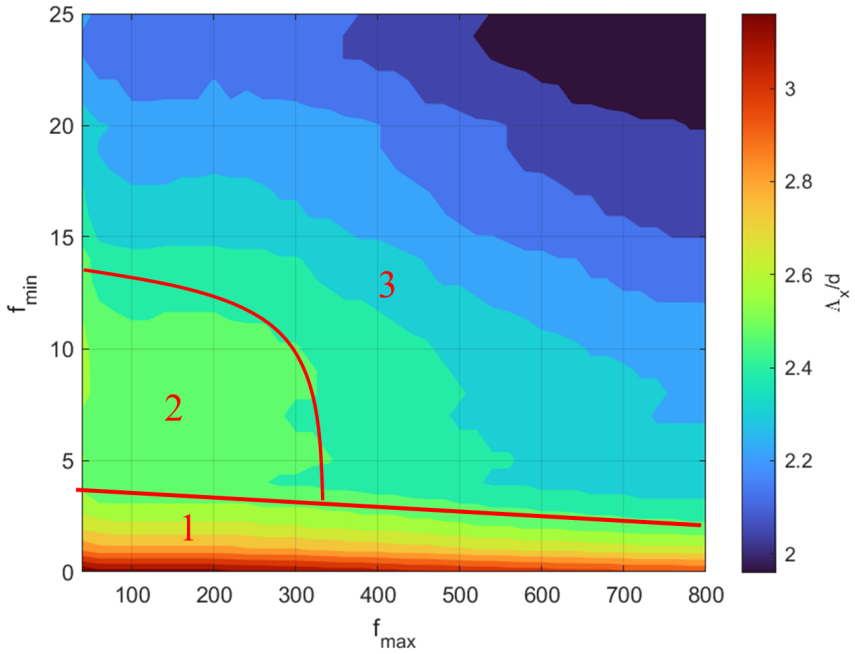

Figure 4.8: Sensitivity of the integral length scale Λ_x/d to the fitting limits $[f_{min}, f_{max}]$.

Region 1 located at very low values of f_{min}, is characterized by high resulting Λ_x. This region is affected by spectral leakage and low frequency inaccuracies which artificially increase the energy of the signal. Increasing f_{max} does not substantially modify this behavior.

Region 2 represents the physically meaningful and numerically stable fitting domain. Here, f_{min} lies within the flat, well-converged portion of the energy-containing range, while f_{max} remains in a frequency range where the negative influence of higher frequencies on the fitting procedure is still moderate.

Region 3 corresponds to combinations where f_{max} extends toward higher frequencies approaching the dissipation range. In this case, progressively larger portions of high-frequency spectral content, irrelevant to the integral scale, are included in the minimization. Although this does not cause abrupt variations, it systematically biases the estimate downward, as the fitting increasingly prioritizes agreement in frequency ranges that do not govern the large scale turbulent motions.

Among the different sources of uncertainty, the selection of the spectral fitting interval represents the dominant contributor to variability when not properly constrained. In this sense, the main source of uncertainty is methodological rather than experimental. However, its impact can be significantly reduced by defining the fitting limits based on physical criteria.

When the entire $(f_{\min}, f_{\max})$ parameter space is considered without constraints, the estimated Λ_x exhibits a variability of approximately ± 2.4 mm (P5–P95 range), highlighting the strong dependence of the result on arbitrary choices of the fitting bounds. A systematic exploration of the parameter map, however, reveals a broad intermediate plateau (Region 2) in which Λ_x becomes nearly invariant. This region spans approximately $f_{\min} \in [3, 10]$ Hz and $f_{\max} \in [80, 300]$ Hz, although its boundaries are not sharp. Within this domain, the mean value of Λ_x is 15.01 mm and the P5–P95 variability reduces to approximately ± 0.28 mm, an order-of-magnitude decrease compared to the unconstrained case.

The extent and existence of this plateau indicates structural stability. If an analogous sensitivity analysis were performed on the averaging limits used in the conventional zero-frequency extrapolation method (Eq. 2.33), such a plateau would not emerge. Instead, the estimate would exhibit a strong dependence on the upper frequency bound f_{max}, with a continuous decrease of Λ_x as $f_{\max}$ increases, and no identifiable region of invariance (see Fig. 4.2a).

Once the fitting limits are selected accordingly, the results obtained with the proposed procedure (Section 5.1) are consistent with those from conventional methods, while exhibiting significantly reduced variability.

4.3. Uncertainty analysis

Once the fitting parameters are established, the methodological sensitivity associated with the choice of the spectral fitting interval is effectively constrained. At this stage, the remaining uncertainty contributions can be examined.

The uncertainty associated with the estimation of the integral length scale can be separated into two distinct contributions: measurement uncertainty and statistical uncertainty. While the measurement uncertainty originates from the experimental process itself, including calibration errors and uncertainties in the flow properties, the statistical uncertainty arises from the finite duration of the velocity time series and reflects the limited statistical convergence of the turbulent signal.

4.3.1. Statistical uncertainty

As discussed by Boufidi et al. [5], short acquisition times limit the statistical convergence of turbulence parameters, particularly those governed by the low frequency content of the spectrum, such as the integral length scale. Since the estimation of Λ_x depends on the proper resolution of the energy-containing range and the convergence of the spectrum as $f \to 0$, insufficient signal duration leads to larger variability and wider confidence intervals. Increasing the acquisition time improves the convergence of the low frequency spectral content, increases the number of statistically independent large-scale structures captured in the record, and consequently reduces the statistical uncertainty of the length scale estimate, while the measurement uncertainty remains essentially unaffected.

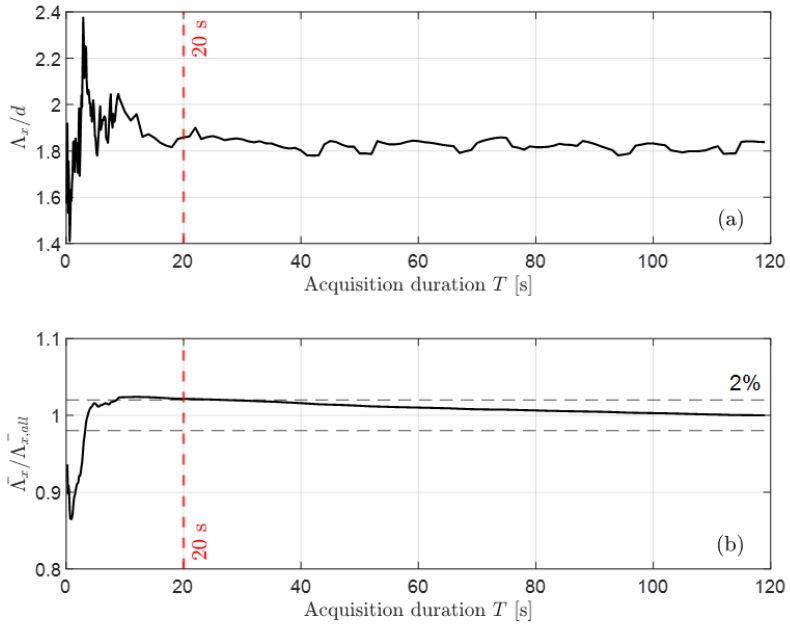

Figure 4.9: Convergence of the integral length scale Λ_x/d as a function of acquisition duration. (a) Instantaneous estimate of Λ_x/d. (b) Normalized cumulative mean $\bar{\Lambda}_x(T)/\bar{\Lambda}_{x,\mathrm{all}}$.

Ideally, the identification of a suitable acquisition time would require several independent measurements performed under identical test conditions at different signal durations. The appropriate duration could then be defined as the minimum time for which the estimated length scale exhibits limited variability and approaches a stable value.
Rather than performing multiple independent experiments, a single long acquisition was recorded at a fixed sampling frequency of $F_s = 100\,\mathrm{kHz}$. Subsignals with progressively longer time durations were extracted and processed independently. In this way, the convergence behavior of the integral length scale Λ_x was evaluated as a function of signal

duration, allowing the minimum acquisition time required for a stable estimate to be identified.

Figure 4.9 shows the evolution of the estimated integral length scale as a function of acquisition duration T. Panel (a) reports the instantaneous estimate of Λ_x/d, while panel (b) shows the cumulative mean $\bar{\Lambda}_x(N)$ normalized by the global mean computed over the entire record, $\bar{\Lambda}_{x,all}$.

For small durations a transient behavior is observed, followed by progressive stabilization of Λ_x. Beyond approximately $T \approx 20s$, the normalized cumulative mean remains within 2% of the global average, indicating that the contribution of additional samples produces only marginal variations in the estimated integral length scale.
Under the present experimental conditions, a signal duration of 20 s was therefore selected, as it provides satisfactory statistical convergence of Λ_x while keeping the overall testing time within reasonable limits.

Such analysis is feasible in a continuous operating facility, like the one employed in this campaign, where long stationary signals can be acquired. In contrast, for facilities with constrained test durations (e.g., blow-down wind tunnels), the uncertainty associated with limited acquisition times cannot be reduced by extending the measurement. In such cases, the statistical uncertainty can be quantified using the moving block bootstrap (MBB) method, a nonparametric resampling algorithm described by Boufidi et al. [5], which provides confidence intervals accounting for the finite length of the velocity time series.

4.3.2. Measurement uncertainty

The third major factor affecting the accuracy of the integral length scale and turbulence statistics is the propagation of measurement uncertainty. This uncertainty originates from two distinct phases: the hot wire calibration phase, specifically within the $Re = f(Nu)$ relationships and the angular calibration $\alpha = f(Re_1/Re_2)$, and the subsequent measurement and post-processing phase.

Initially, the uncertainty inherent in the calibration process was evaluated. During the calibration performed with the *Dantec StreamWare* software, uncertainties in the primary quantities provided by the automatic calibrator were propagated based on manufacturer specifications. These values are summarized in Table 4.2. Following the methodology of Boufidi [4], hardware parameters such as wire length (l_w), wire diameter (d_w), bridge resistances, and wire temperatures were considered constant and therefore not treated as stochastic variables in the analysis.

Table 4.2: Instrumental uncertainties during the calibration phase (1-σ).

Parameter (Calibration)	**Symbol**	**Uncertainty (1-σ)**
Ambient Pressure	$u_{P_{cal}}$	20 Pa
Stagnation Temperature	$u_{T_{0,cal}}$	0.5 K
Reference Velocity	$u_{U,cal}$	0.02 m/s
Bridge Voltage	$u_{E_b,cal}$	0.001 V [5]

For the $Nu-Re$ curves of both wires, a Taylor Series expansion was employed to evaluate the bias limit of the calculated Reynolds number ($u_{Re,bias}$) and, following an identical procedure, the bias limit for the Nusselt number ($u_{Nu,bias}$):

$$u_{Re,bias} = \sqrt{\sum \left(\frac{\partial Re}{\partial x_i} u_{x_i} \right)^2} = \sqrt{\left(\frac{\partial Re}{\partial P_{cal}} u_{P_{cal}} \right)^2 + \left(\frac{\partial Re}{\partial T_{0,cal}} u_{T_{0,cal}} \right)^2 + \dots} \tag{4.1}$$

The sensitivity coefficients explicitly account for functional dependencies of the fluid properties, such as $k = f(T)$ and $\mu = f(T)$. These analytical bias limits were then combined with the statistical interpolation error (u_{fit}), representing the Standard Estimate of Error (SEE) of the residuals, to determine the total uncertainty of the calibration curves:

$$u_{Re,total} = \sqrt{u_{fit}^2 + u_{Re,bias}^2 + \left(\left| \frac{\partial Re}{\partial Nu} \right| \cdot u_{Nu,bias} \right)^2} \tag{4.2}$$

This approach was applied to propagate the uncertainties for both wires and subsequently for their ratio as a function of the flow angle $\alpha = f(Re_1/Re_2)$, leading to 95% expanded confidence intervals ($\pm 2\sigma$) of ± 0.15 for Re_1, ± 0.13 for Re_2, and $\pm 1.7°$ for the angular calibration α. The resulting 95% expanded confidence intervals for the $Nu_1 - Re_1$ and angular calibrations are reported in Fig. 4.10 (a) and (b), respectively.

To bypass the analytical difficulty of propagating these errors through the non-linear trigonometric reconstructions and spectral estimations required for the estimation of Λ_x, a Monte Carlo Method (MCM) was implemented in the post-processing phase. In this stage, uncertainties related to the actual measurement conditions, including flow temperature, air density, and the angular positioning of the probe, were introduced (Table 4.3). These variables represent the fundamental quantities required to convert the Nusselt and Reynolds numbers into physical velocity fluctuations. Furthermore, the total uncertainty of the calibration curves, previously derived during the calibration phase, was included in the stochastic model.

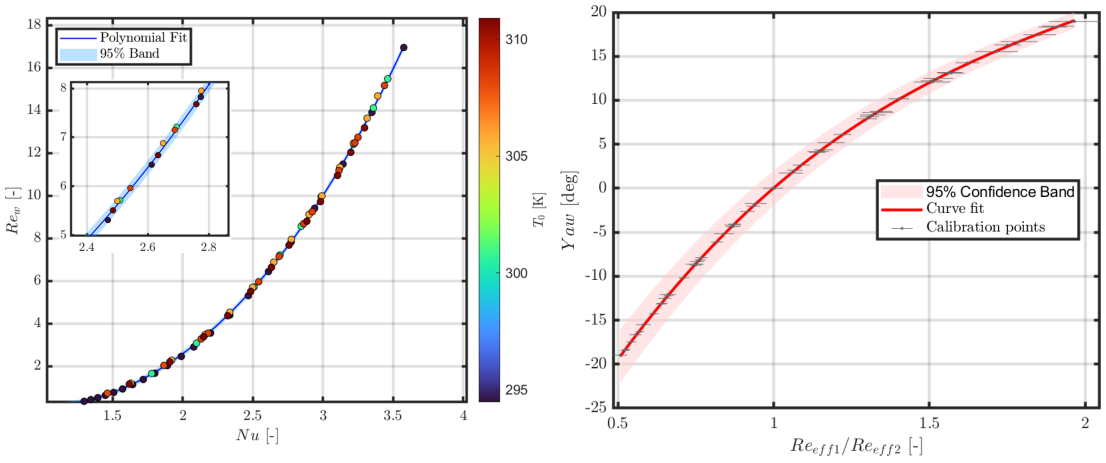

(a) (b)

Figure 4.10: Calibration uncertainty analysis for the (a) Nu–Re and (b) angular response curves with 95% expanded confidence band.

Table 4.3: Instrumental and calibration uncertainties introduced in the measurement phase (1-σ).

Parameter (Measurement)	**Symbol**	**Uncertainty (1-σ)**
Flow Temperature	$u_{T_{0,meas}}$	0.25 K
Bridge Voltage	$u_{E_b,meas}$	0.001 V [5]
Air Density	u_ρ	0.002 kg/m^3
Angular Positioning	u_θ	0.2 deg
Wire 1 Calibration	σ_{Re_1}	0.075
Wire 2 Calibration	σ_{Re_2}	0.065
Angular Calibration	σ_α	0.85 deg

For a representative experimental data point, the measurement was re-processed $N = 10000$ times. In each iteration j, the nominal calibration laws and the accessory measurement variables were perturbed by random Gaussian samples. For a generic variable or calibration fit Φ, the perturbed value Φ_j is defined as:

$$\Phi_j = \Phi + \mathcal{N}(0, \sigma_\Phi) \tag{4.3}$$

This stochastic process generates a probability density function (PDF) for every calculated quantity, including turbulence intensity Tu, and integral length scales Λ_x. The process was repeated across the range of experimental conditions investigated in Chapter 5. The resulting distributions were found to be nearly identical for all tests, characterized by a near-Gaussian shape.

Examples of the resulting PDFs for Tu and Λ_x are reported in Fig. 4.11. Specifically for Λ_x, the sensitivity to calibration bias resulted in an expanded uncertainty of $\pm 0.62\ mm$. It is crucial to highlight that the uncertainty computed for the Λ_x is based on a prior optimal tuning of the length scale estimation parameters (as discussed in Section 4.2.4). Consequently, these results should be interpreted as the unavoidable effect that calibration and measurement uncertainty have on the results obtained after the methodology has been optimally tuned. As such, this value represents the physical limit of the measurement's precision rather than an error introduced by sub-optimal parameter selection.

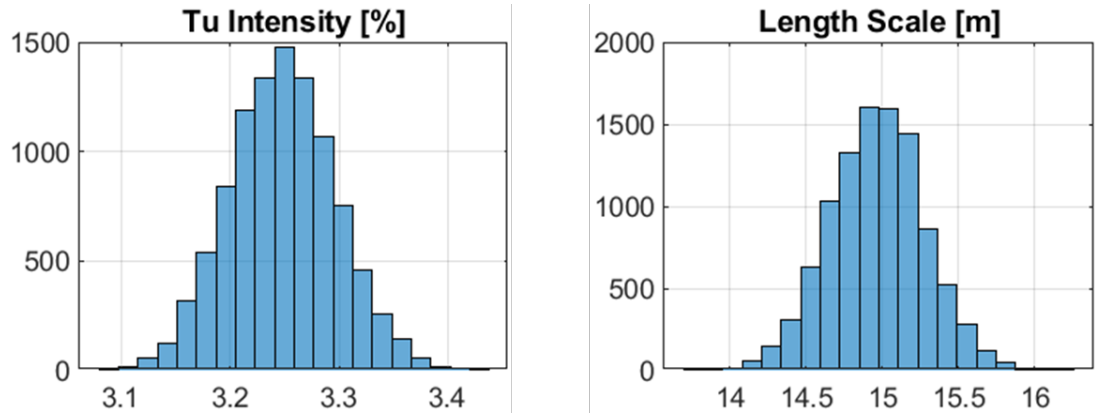

Figure 4.11: (a) Histogram of turbulence intensity (Tu). (b) Histogram of integral length scale.

5| Experimental results

This chapter presents the experimental results of the integral length scale obtained using the proposed methodology under different test cases. The estimated values are compared with those provided by conventional formulations in order to assess the consistency and physical reliability of the approach.
For all the test cases considered, the degree of isotropy was experimentally verified, with the isotropy ratio ranging between 1.04 and 1.20. According to Roach [28], these values indicate near-homogeneous and nearly isotropic turbulence conditions.

The validation process is structured in two stages. First, the method is evaluated on the reference test case used during its development, with particular attention to repeatability and test-to-test variability under identical operating conditions.
Finally, the methodology is applied to independent test configurations, including different turbulence grid arrangements and off-design operating conditions. This broader validation aims to verify the generality and stability of the proposed approach when applied to flow conditions that differ from those used for its development.

5.1. Validation on the reference test case

Experimental results illustrating the downstream evolution of the normalized integral length scale, Λ_x/d, for grid A (described in Fig. 3.3) operating in passive mode are shown in Fig. 5.1. The integral scales obtained using the developed iterative procedures based on the von Kármán and Pope spectral models are compared with values derived from conventional approaches, namely, the autocorrelation based method (Eq. 2.10) and the zero-frequency spectral extrapolation method proposed by Roach [28] (Eq. 2.33). The data are also benchmarked against the experimental correlations reported by Bertelli et al. [3] and Roach [28] (see Fig. 5.1).

Consistent with the discussion in Section 4.1, the integral scales estimated via autocorrelation are systematically larger than those obtained from spectral-based approaches. This

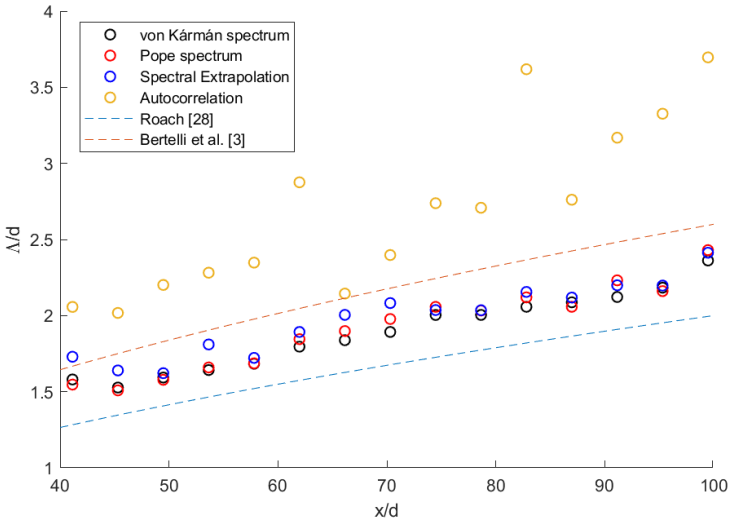

Figure 5.1: Downstream evolution of the normalized integral length scale Λ_x/d as a function of the normalized distance x/d for grid A. Results obtained using different estimation approaches are compared with the empirical correlations proposed by Bertelli et al. [3] and Roach [28].

behavior arises from the sensitivity of autocorrelation-based estimates to low-frequency content, which tends to artificially inflate the integral scale. As a consequence, this method yields significantly higher values that deviate from both the empirical correlations and the physically consistent downstream trend observed under the present experimental conditions.

In contrast, spectral based approaches allow the fitting or averaging interval to be selected within the physically meaningful energy containing range, thus excluding problematic low frequency components. In the present study, for example, the zero-frequency extrapolation method was applied by averaging the spectrum over the interval $[5, 30]$ Hz. This range was selected to remain within the energy containing region while avoiding the lowest frequency disturbances.

A similar filtering strategy could in principle be applied to the autocorrelation method by introducing a high-pass filter to remove low frequency content prior to integration. In practice, applying progressively higher cut-off frequencies indeed leads to a reduction of the estimated integral length scale. However, this reduction does not converge: the estimated value continues to decrease as increasingly larger portions of the low frequency spectrum are removed. This behavior reflects the fact that the integral length scale is inherently governed by the largest turbulent structures, which are associated with low frequency content. Consequently, an arbitrary high-pass filtering procedure risks excluding physically relevant contributions and artificially modifying the signal.

Unlike the spectral fitting approach, the autocorrelation method provides no objective criterion for selecting an appropriate high-pass cut-off frequency. The absence of such guidance introduces subjectivity and may lead to excessive data manipulation, effectively altering the physical content of the measurement.

As showed in Fig. 5.1 all spectrum based methods provide mutually consistent results. The iterative procedures developed in this work closely reproduce both the magnitude and downstream trend predicted by the correlations. Notably, the agreement between results obtained using the von Kármán and Pope spectral formulations demonstrates the robustness of the proposed methodology, independently of the specific spectral model adopted. In the present study, the von Kármán spectrum has been preferred due to its relative simplicity compared to the parametric Pope model, which requires tuning of model constants to the specific flow conditions.
Furthermore, the developed approach shows excellent agreement with the conventional zero-frequency extrapolation method, while avoiding the arbitrary selection of the low-frequency averaging range required in that procedure. This feature is demonstrated in Fig. 5.2a, which represents the envelope of Λ_x/d values obtained by applying the extrapolation method averaging the spectrum between $f_{\min} = 5\,\text{Hz}$ and $f_{\max}$ swept within the energy-containing range $(5 - 45\,\text{Hz})$. The shaded band highlights the sensitivity of this spectral based method to the choice of the averaging interval, whereas the von Kármán-based iterative results lie within this envelope, confirming consistency while providing a more robust and objective evaluation of the integral length scale.

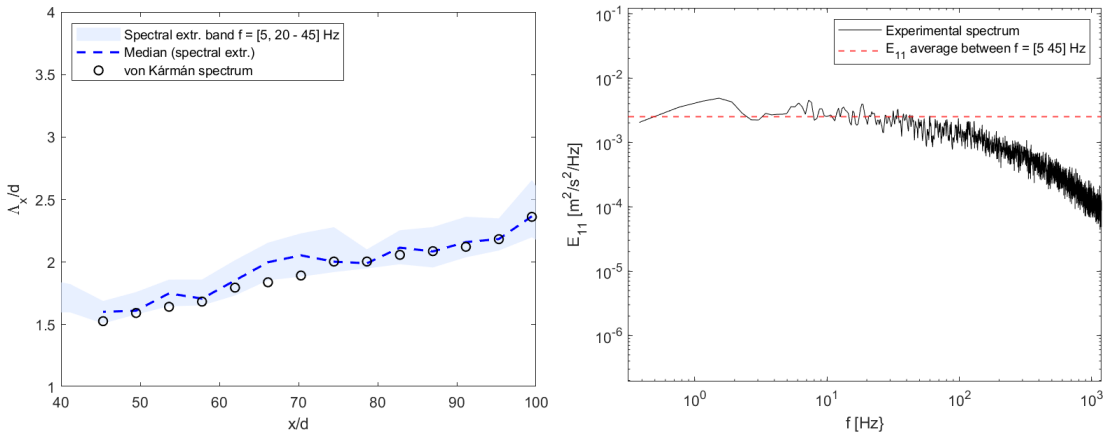

(a) (b)

Figure 5.2: (a) Λ_x/d versus x/d. Shaded region: spectral extrapolation results (f_{min} = 5 Hz, f_{max} varied in the energy-containing range) compared with the von Kármán fit. (b) Example spectrum $E_{11}(f)$ with the widest averaging band [5, 45] Hz used for zero-frequency extrapolation.

5.1.1. Repeatability assessment

In this section, the results from two separate tests performed under identical operating conditions are compared in order to assess the test-to-test variability of the different estimation methods. As shown in Fig. 5.3, the autocorrelation-based method exhibits the largest dispersion between the two datasets, indicating a significantly higher variability. This behavior is quantitatively confirmed by the higher values of the standard deviation of the difference between corresponding length scales from each test Δ, std(Δ), as well as by the coefficient of variation, $CV\%$, defined as the ratio of std(Δ) to the mean of all estimated length scales.

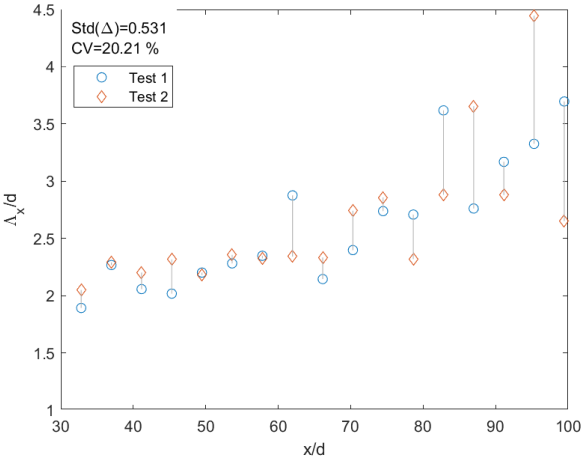

(a) Autocorrelation

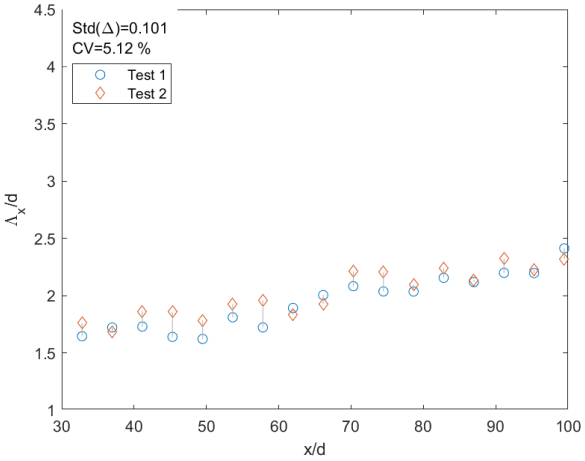

(b) Spectral extrapolation

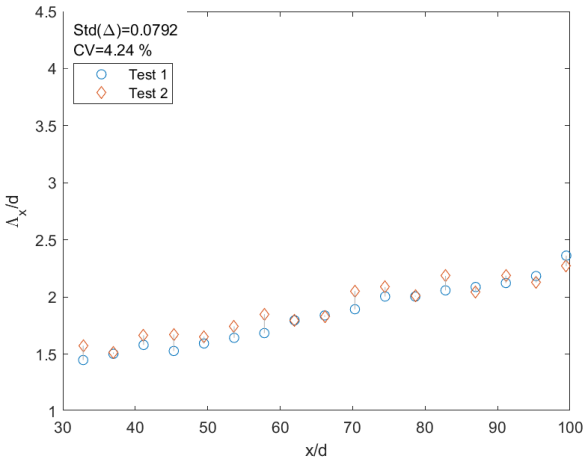

(c) Von Karman spectrum iterative method

Figure 5.3: Repeatability analysis of the three estimation methods. The reported metrics are Std(Δ) and $CV\%$.

In contrast, the spectral-based approaches demonstrate much smaller deviations between

repeated tests. The differences between the two measurements remain limited over the entire range of x/d, resulting in substantially lower standard deviation and coefficient of variation values. This indicates a higher level of repeatability and robustness for the spectral methods under identical test conditions.

Overall, the comparison highlights that while all methods capture the general trend of Λ_x along x/d, the spectral-based techniques provide more stable and repeatable estimates, whereas the autocorrelation method appears more sensitive to test-to-test fluctuations. Among the spectral approaches, the von Kármán based method yields the lowest coefficient of variation (4.24%), compared to 5.12% for the spectral extrapolation method, indicating a moderate improvement in test-to-test repeatability.

5.2. Validation across different test configurations

In this second part, the procedure described in Chapter 4 is applied to different test cases following the steps below. First, the spectrum at a representative acquisition point during the decay is inspected to identify the approximate frequency ranges that delimit the energy containing range and the inertial subrange. It is shown that these ranges do not depend on turbulence intensity, but change with the Reynolds number.
Next, the fitting interval $[f_{min}, f_{max}]$ is swept across the spectrum, varying both limits within the bounds identified previously. A two-dimensional dependence map is then built, and "Region 2" is identified and delimited as the area where the estimated Λ_x is most stable, i.e., least affected by both low-frequency and high-frequency biases in the fitting procedure.
Once Region 2 is selected, the variability of the results within that area is quantified, providing an estimate of the methodological uncertainty associated with the choice of fitting limits. After the fitting limits are fixed for one acquisition point, the same limits can be used to process the full dataset, provided that the flow remains isotropic and homogeneous and the test conditions (e.g., Reynolds number) are unchanged. If the spectral ranges shift, the fitting limits must be updated accordingly.

5.2.1. Alternative turbulence grid configuration

This test case is meant to demonstrate the length scale estimation procedure for the dataset acquired using grid B. Compared to grid A, grid B has the same solidity (i.e., the fraction of blocked area), approximately 33% and the same geometry, but it has a larger bar diameter. This enables higher turbulence intensities and larger streamwise integral length scales Λ_x. Having a second grid expands the experimentally achievable (Tu, Λ_x)

combinations and helps to decouple turbulence intensity from length scale. The active mode can further modulate these two parameters more independently.

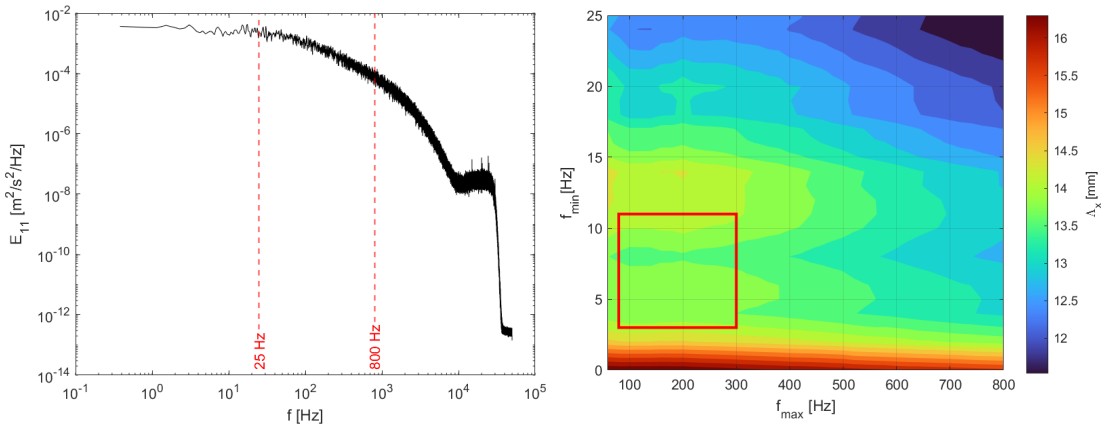

(a) (b)

Figure 5.4: (a) Power spectral density $E_{11}(f)$ The dashed red lines indicate the approximate bounds of the investigated f_{min}, f_{max}; (b) Two-dimensional dependence map of the estimated Integral length scale as a function of $[f_{min}, f_{max}]$, The red rectangle highlights Region 2, where Λ_x is the most stable.

Figure 5.4a displays the experimental spectrum obtained for a turbulence intensity of 6.4% with the approximate frequencies limiting the energy containing range and the inertial subrange. The fitting interval $[f_{min}, f_{max}]$ is swept within these ranges and the results are presented in Fig. 5.4b.

In contrast to the previous case, region 2 was deliberately defined using the same frequency bounds adopted for Grid A in Section 4.2.4, namely $f_{\min} \in [3, 11]$ Hz and $f_{\max} \in [80, 300]$ Hz. This choice was made intentionally to assess whether the fitting interval identified for the reference configuration could be retained without further adjustment when changing grid geometry and turbulence intensity. In other words, the objective was to verify the robustness and transferability of the selected fitting range, rather than re-optimizing it for each configuration.

The results confirm that this assumption is justified. In region 2, the variability of Λ_x, quantified by the P5–P95 percentile range $[13.67, 14.20]$ mm, remains limited and comparable to that obtained for Grid A. This indicates that the same fitting interval provides equally consistent estimates of the integral length scale, despite the different turbulence conditions. Therefore, the sweep procedure does not need to be repeated for this configuration: the previously identified frequency bounds can be retained without loss of accuracy.

Within Region 2, the estimated streamwise integral length scale is

$$\Lambda_x = 13.94 \pm 0.26 \; mm$$

where the reported spread reflects the methodological sensitivity of the estimation procedure to the selected fitting interval, rather than the measurement uncertainty.

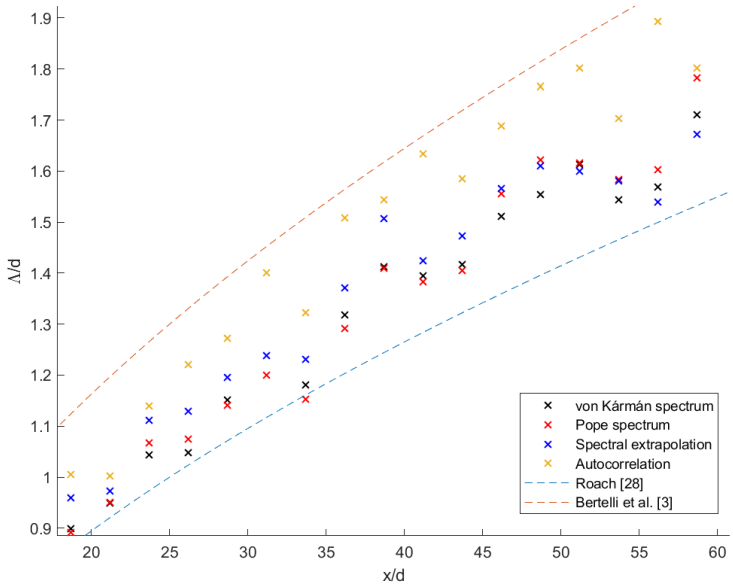

Figure 5.5: Downstream evolution of the normalized integral length scale Λ_x/d as a function of the normalized distance x/d for grid B. Results obtained using different estimation approaches are compared with the empirical correlations proposed by Bertelli et al. [3] and Roach [28] for passive grids.

The resulting integral length scales estimated from this dataset using the different methods are presented and compared in Fig. 5.5, together with the experimental correlations proposed by Roach [28] and Bertelli et al. [3]. The results obtained with the autocorrelation method appear significantly more stable and more consistent with those derived from the spectral method than in the case of grid A (see Fig. 5.1). This difference can be attributed to the lower low-frequency disturbances present in the spectra of the grid B dataset.

This behaviour becomes evident when comparing the spectra of the two grids, as shown in Fig. 5.6. The spectrum obtained for grid A exhibits a stronger low-frequency amplification, which directly affects the autocorrelation function and, in particular, the location of its zero-crossing.
It should be noted that the two spectra correspond to different turbulence intensities, namely 3.3% and 6.4% for grid A and grid B, respectively. For comparison, the spectra

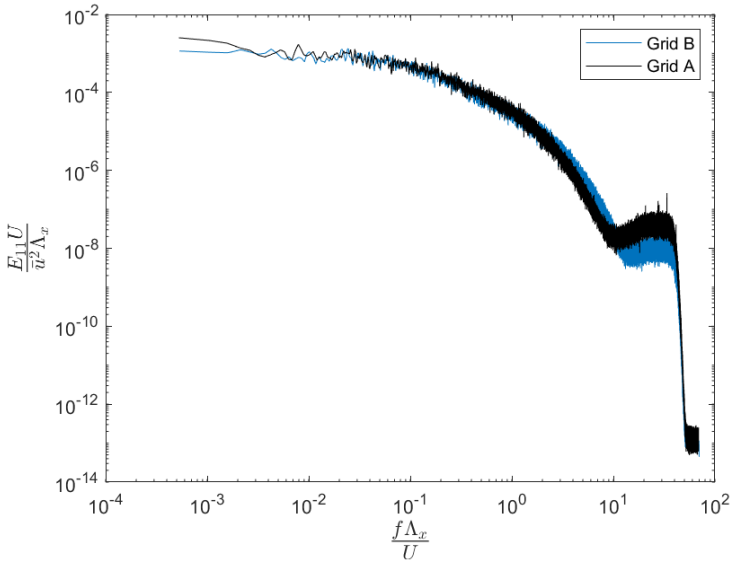

Figure 5.6: Comparison of the non-dimensionalized streamwise power spectral density for grid A and grid B. The spectra correspond to turbulence intensities of 3.3% (grid A) and 6.4% (grid B), respectively.

are presented in non-dimensional form. This normalization is performed using the integral length scale calculated with the proposed iterative method, which successfully collapses the two curves. This further supports the internal consistency and physical reliability of the proposed estimation procedure.

Although this dataset is less affected by low-frequency disturbances, the results obtained using the autocorrelation based method systematically yield higher integral length scale values than those derived from the spectral based approach, confirming the general tendency previously observed for this method.
As discussed for the reference test case, the developed iterative procedure, based on both the von Kármán and Pope spectral formulations, shows very good agreement with the integral length scale estimated through the zero-frequency extrapolation of the spectrum. The proposed methodology is therefore demonstrated to be consistent and physically reliable also for the present dataset.

5.2.2. Off-design operating conditions

When the test is conducted under off-design Reynolds number conditions, the measured spectrum shifts toward higher frequencies. This behaviour can be interpreted in light of Taylor's frozen turbulence hypothesis (Eq. 2.23), which establishes a direct relationship between temporal frequency and spatial scales. For a given turbulent structure, an

increase in the mean flow velocity results in a proportional shift of the corresponding spectral content toward higher frequencies.

As a consequence, while it is acceptable to retain the same fitting interval for the alternative grid configuration under similar flow conditions, a new $[f_{\min}, f_{\max}]$ sensitivity analysis is required when operating at different Reynolds numbers. This ensures that the selected fitting range remains consistent with the energy-containing and inertial subranges of the spectrum.

The off-design tests were performed at an exit isentropic Reynolds number, calculated with the axial chord as described in Section 3.5, twice that of the reference case (160000 compared to 80000) with grid A. Accordingly, the frequencies delimiting the energy-containing range and the inertial subrange are expected to shift approximately to twice the values selected in the baseline configuration (Fig. 5.7a).

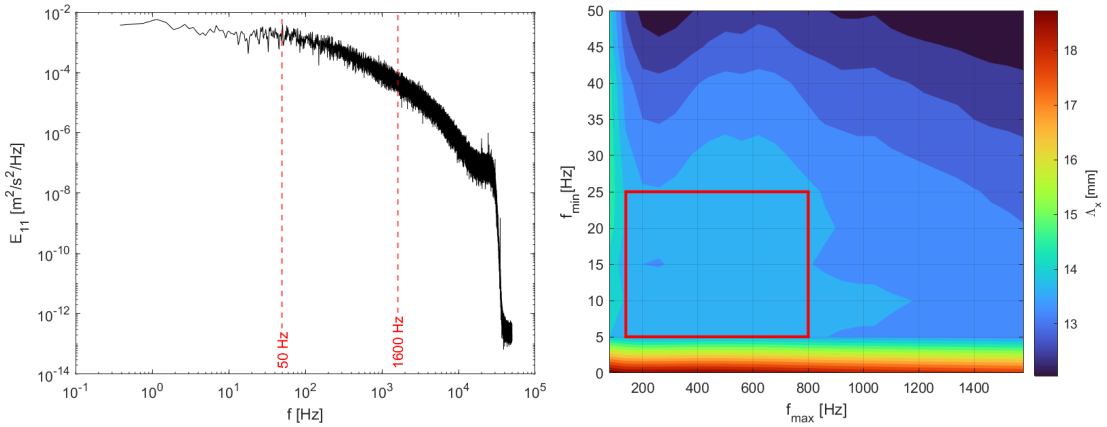

(a) (b)

Figure 5.7: (a) Power spectral density $E_{11}(f)$ The dashed red lines indicate the approximate bounds of the investigated f_{min}, f_{max}; (b) Two-dimensional dependence map of the estimated Integral length scale as a function of $[f_{min}, f_{max}]$, The red rectangle highlights Region 2, where Λ_x is the most stable.

Figure 5.7b shows the two-dimensional dependence map of the estimated integral length scale as a function of $[f_{\min}, f_{\max}]$. In this case, a significantly wider stable region of Λ_x, marked with a red rectangle, can be identified. Overall, the spectrum obtained at higher Reynolds number exhibits a broader and more stable energy-containing range, resulting in a more robust fitting procedure and a more reliable estimate of the integral length scale. Within the stable region identified with $f_{\min} \in [5, 25]$ and $f_{\max} \in [140, 800]$ Hz, the integral length scale is

$$\Lambda_x = 13.77 \pm 0.148 \; mm$$

where the uncertainty related to the methodological sensitivity corresponds to the sensitivity band defined by the P5–P95 percentile range $[13.63, 13.93]$ mm obtained by sweeping the fitting interval inside the red rectangle.

The downstream decay of the normalized integral length scale obtained under off-design Reynolds number conditions is reported in Fig. 5.8, where the results are compared with the different estimation methods and with the empirical correlations.
In this dataset, the conventional spectral zero-frequency extrapolation method yields higher integral length scale values, approaching those obtained through the autocorrelation based approach. The zero-frequency extrapolation was performed by averaging the spectrum over the interval $[5, 60]$ Hz. The upper bound of this interval was doubled with respect to the nominal Reynolds number case, consistently with the expected frequency shift discussed previously based on Taylor's hypothesis.

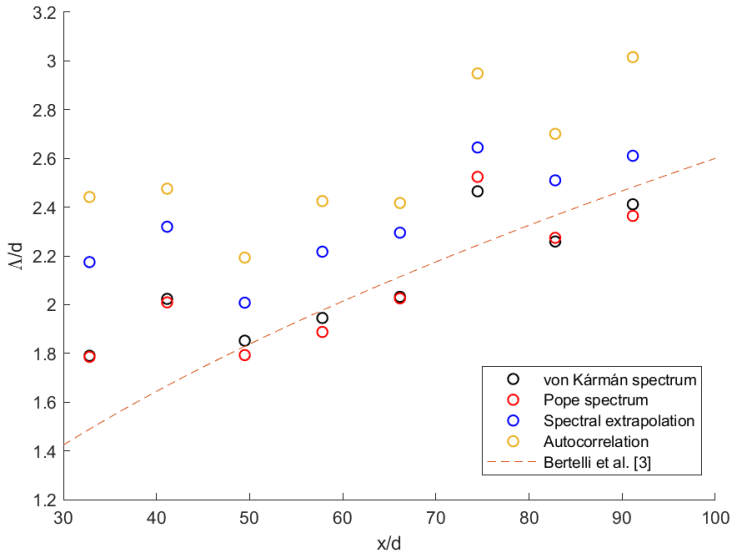

Figure 5.8: Downstream evolution of Λ_x/d as a function of the normalized distance x/d in off-design Reynolds conditions obtained using different estimation approaches.

However, a closer inspection of selected spectra along the decay (see Fig. 5.9a) reveals the presence of fluctuations beyond approximately 25 Hz. These fluctuations increase the average spectral level within the selected interval, thus artificially elevating the zero-frequency extrapolated estimate of Λ_x. In contrast, the von Kármán spectral fitting procedure remains less sensitive to such local fluctuations, as it constrains the fit over the physically consistent energy-containing and inertial ranges.
This behaviour explains the larger discrepancy observed between the conventional spectral method and the proposed iterative approach under off-design conditions, and further supports the robustness of the fitting-based methodology.

In order to assess the influence of the averaging interval, the decay was reprocessed using a restricted frequency range $[5, 25]$ Hz for the zero-frequency extrapolation. The resulting integral length scales are shown in Fig. 5.9b.

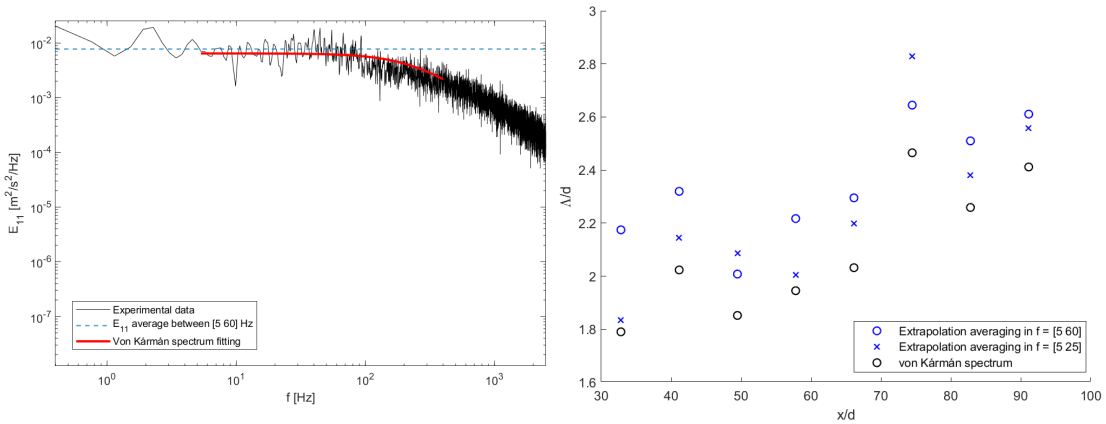

(a) (b)

Figure 5.9: (a) Example of power spectral density used for the zero-frequency extrapolation under off-design conditions. (b) Comparison of the downstream decay of Λ_x/d obtained using zero-frequency extrapolation with two averaging intervals, $[5, 60]$ Hz and $[5, 25]$ Hz, together with the von Kármán fitting results.

When the upper limit of the averaging interval is reduced, the conventional spectral estimates become comparable with those obtained from the von Kármán fitting procedure. This confirms that the previously observed overestimation was not related to the physical evolution of the turbulence scales, but rather to the sensitivity of the zero-frequency extrapolation to spectral fluctuations at intermediate frequencies.
The comparison clearly highlights the intrinsic variability of the zero-frequency method with respect to the chosen averaging interval. Modifications of the frequency window lead to measurable changes in the estimated integral length scale. In contrast, the fitting-based approach remains substantially less sensitive to such variations, demonstrating greater robustness.

Finally, a direct comparison between the two Reynolds number conditions, both processed using the von Kármán spectral fitting procedure, is presented in Fig. 5.10. The off-design case ($Re_{2,is} = 160000$) exhibits higher normalized integral length scale values compared to the reference condition ($Re_{2,is} = 80000$) over the entire downstream range.

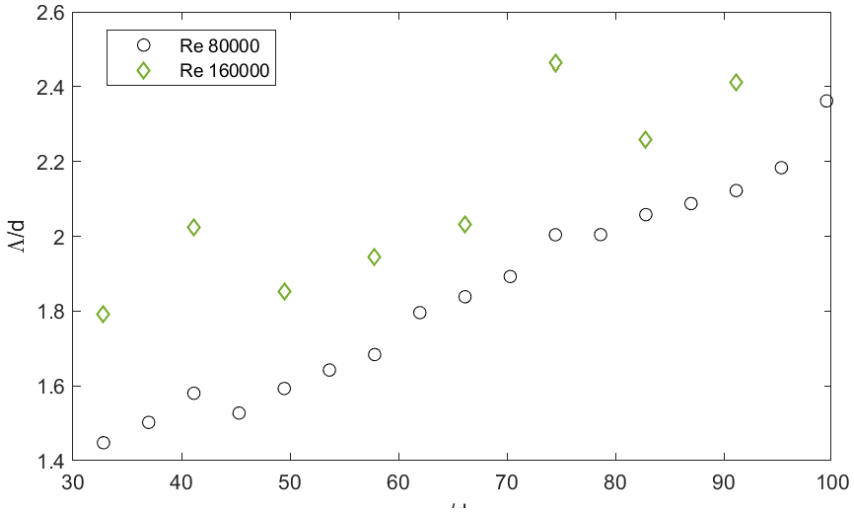

Figure 5.10: Comparison of Λ_x/d obtained using the von Kármán spectral fitting at $Re = 80000$ and $Re = 160000$.

5.2.3. Active grid configuration

The analysis is now extended to the active grid configuration in order to assess how the introduction of jet injection modifies the turbulence structure with respect to the passive case. While the passive grid generates turbulence solely through wake formation and bar induced blockage, the active grid introduces additional momentum through the injection system altering both the effective blockage and the wake development downstream of the bars.

The test case considered in this section corresponds to Grid A operating in simultaneous injection mode with a 2% injection rate. This configuration represents a mild active condition, where the injected jet modifies the wake development and the effective blockage of the grid, leading to measurable changes in the turbulence structure and in the resulting integral length scales.

The objective of this analysis is to verify that the proposed estimation methodology remains consistent and robust under active grid conditions. In particular, the aim is to assess whether the developed spectral fitting procedure provides stable and physically consistent integral length scale estimates even when the turbulence field is altered by active injection. The downstream evolution of Λ_x is therefore compared with both the passive configuration and the empirical correlation proposed by Bertelli et al. [3], in order to confirm that the method captures the expected trends without loss of reliability.

Inspection of the colormap indicates that the resulting Λ_x values obtained through the frequency sweep are relatively stable over the entire map, with an overall variability of

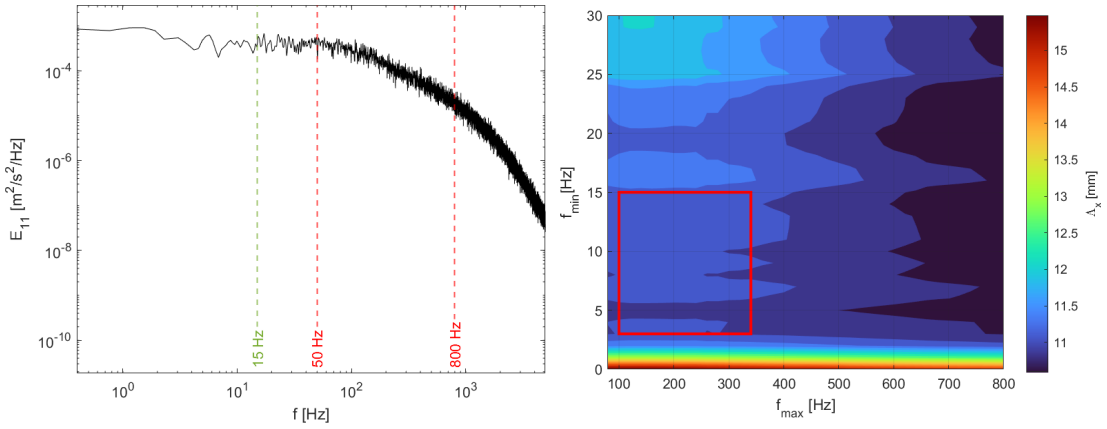

(a) (b)

Figure 5.11: (a) Power spectral density $E_{11}(f)$. The dashed red lines indicate the approximate bounds of the investigated f_{min}, f_{max}; (b) Two-dimensional dependence map of the estimated Integral length scale as a function of $[f_{min}, f_{max}]$, The red rectangle highlights Region 2, where Λ_x is the most stable.

± 0.58 mm computed from the P5–P95 percentile range of all estimates. Some fluctuations are observed in the spectrum starting from approximately 15 Hz, indicated with the green dashed line in Fig.5.11a, which introduce a slight increase in the estimated length scale. Nevertheless, the variability in the range 15–30 Hz of f_{min} remains limited, on the order of ± 0.41 mm.

For the subsequent analysis, the fitting interval is therefore restricted to frequencies below 15 Hz, selecting $f_{\min} \in [3, 15]$ Hz and $f_{\max} \in [100, 340]$ Hz. Within this range, the integral length scale is found to be

$$\Lambda_x = 11.13 \pm 0.13 \text{ mm}.$$

The identified frequency range is consistent with that previously obtained for the passive grids at nominal isentropic Reynolds number, confirming that the selection of the fitting interval is primarily governed by the Reynolds number of the flow.

Figure 5.12a shows the downstream evolution of the normalized integral length scale obtained using the different estimation methods. The results are compared with the empirical correlation proposed by Bertelli et al. [3],

$$\frac{\Lambda_x}{d} = D \left(\frac{x}{d} \right)^m$$

where the constants are taken as $D = 0.22$ and $m = 0.45$, within the range originally suggested for the active grid configuration. Overall, the decay trends obtained with the pro-

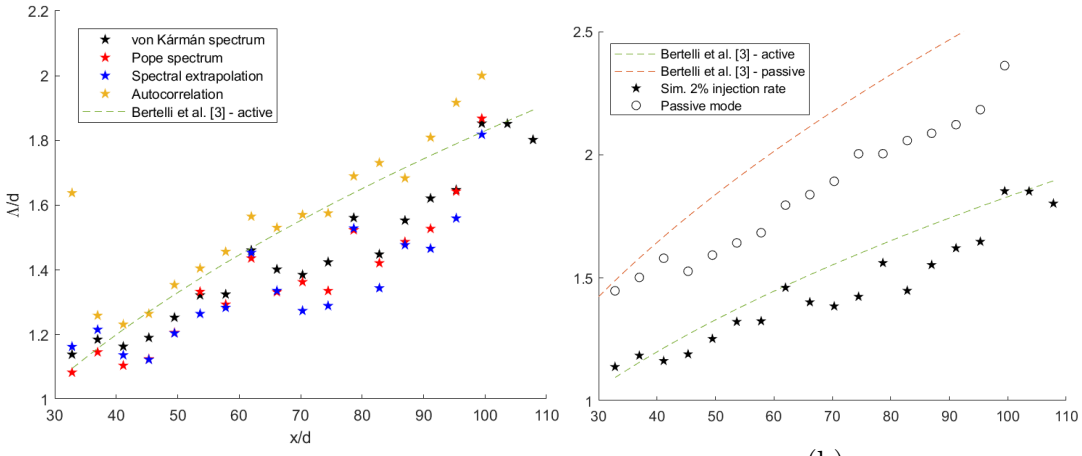

(a) (b)

Figure 5.12: Decay of Λ_x/d as a function of the streamwise distance x/d from the grid (a) Comparison between different estimation methods (b) Comparison between passive mode and 2% simultaneous injection results

posed spectral fitting procedure show very good agreement with the conventional spectral formulation. The downstream growth rate is consistently captured, confirming that the developed method remains reliable even under active injection conditions. This demonstrates that the robustness previously observed for the passive configuration is preserved when the turbulence field is modified by jet forcing.
The values obtained using the autocorrelation-based approach remain systematically higher, as already observed and discussed for the passive grid case. This behavior is consistent with the known sensitivity of the autocorrelation integration to low-frequency contributions and finite-sample effects, which tend to slightly overestimate the integral length scale. Nevertheless, the overall downstream trend remains comparable across all methods, reinforcing the consistency of the proposed estimation strategy.

Figure 5.12b presents a comparison between the passive and simultaneous active grid modes, using the von Kármán iterative method for the length-scale estimation. The results confirm the trend reported by Bertelli et al. [3]: for a low simultaneous injection rate, the normalized integral length scale is consistently lower than in passive mode. This confirms that, at low injection ratios, the added jet momentum modifies the wake structure and promotes mixing, leading to smaller characteristic turbulence scales while preserving the downstream power-law growth trend.

5.3. Towards full grid characterization

A comprehensive characterization campaign of the active turbulence grids is currently ongoing at the von Karman Institute. The objective is to map the combinations of turbulence intensity and integral length scale achievable with the available grid geometries and active injection modes. This effort aims at defining the full operational envelope of the turbulence generator in preparation for the experimental campaign on transition and separation phenomena of the C1 SPLEEN low pressure turbine blade.

The characterization includes passive configurations as well as multiple active injection strategies, allowing control over both the effective blockage and the wake development downstream of the bars. The methodology developed in the present work for the estimation of the integral length scale will be consistently adopted throughout the entire measurement campaign, ensuring methodological uniformity and comparability across all configurations.

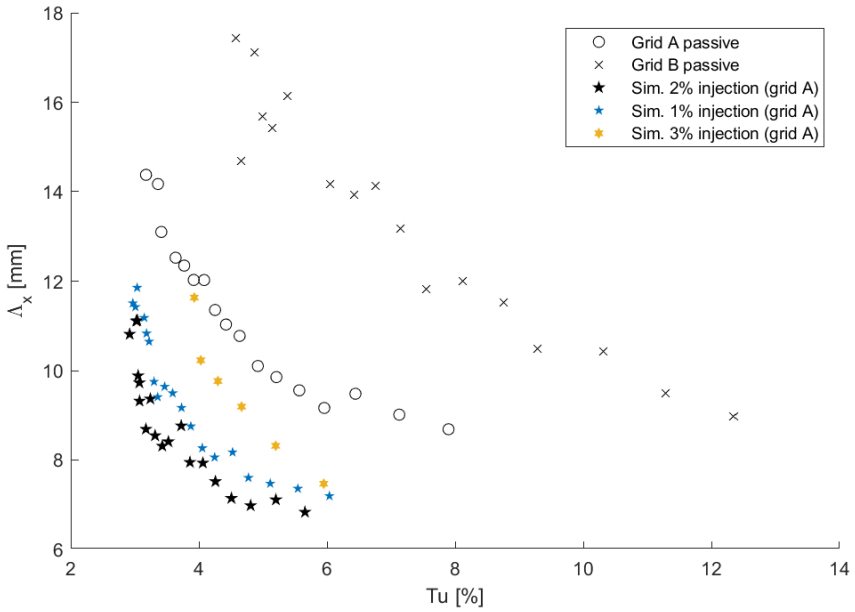

Figure 5.13: Integral length scale Λ_x as a function of turbulence intensity Tu for the different grid configurations and operating modes.

Figure 5.13 presents a preliminary map obtained from a subset of the tested cases, showing the relationship between turbulence intensity and integral length scale. Even at this intermediate stage, the results clearly demonstrate that a broad range of turbulence conditions can be generated. In particular, the data indicate that multiple combinations of turbulence intensity and length scale are attainable, with significant flexibility in independently varying these parameters.

This capability is essential for systematically investigating the boundary layer response of the turbine blade under controlled free-stream turbulence conditions. The availability of distinct length scales at comparable turbulence intensity levels provides the necessary degrees of freedom to isolate and study the effects of turbulence structure on transition and separation mechanisms.

6| Conclusions

This work focused on the experimental estimation of the integral length scale, a fundamental turbulence descriptor in turbomachinery research, where accurate inflow characterization is essential for the physical interpretation of experimental results and for CFD validation.

The study successfully identified and validated a robust alternative to conventional length scale estimation techniques. The method can serve as a practical guideline for length scale characterization not only within the present experimental campaign, but also in other facilities and under different operating conditions.

The proposed iterative approach can be interpreted as a structured zero-frequency extrapolation of the spectrum. Classical low frequency extrapolation typically lacks objective criteria for selecting the extrapolation range and procedure, making the final estimate sensitive to user-dependent choices. By relying on analytical spectral models (von Kármán and Pope formulations), the present method places the extrapolation within a consistent theoretical framework, providing a more controlled and repeatable estimation process. This structured implementation reduces variability associated with subjective methodological decisions and leads to improved repeatability between tests performed under identical conditions. It must be emphasized that the applicability of the proposed methodology is linked to the validity of Kolmogorov's similarity hypotheses. The method assumes the presence of a well-defined inertial subrange with a clear spectral decay consistent with high Reynolds number turbulence. Therefore, it can only be applied under conditions in which turbulence is approximately homogeneous and isotropic, and where the Reynolds number is sufficiently high. In flows where these assumptions are not satisfied, the physical basis of the spectral models may no longer hold, limiting the reliability of the iterative procedure.

Among the various sources of uncertainty, the selection of the fitting interval in the spectral domain emerged as the dominant contributor to variability if not properly chosen. However, this work provides physically motivated guidelines for its appropriate selection

based on the identification of the energy-containing and inertial subranges. Once the fitting parameters are consistently defined, the remaining sources of uncertainty, namely statistical and measurement related contributions, can be quantified.

For all the cases investigated, the measurement uncertainty associated with instrumentation and calibration was approximately ± 0.6 mm. The uncertainty related to methodological choices was found to be at most ± 0.3 mm once the fitting intervals were reasonably selected. It is important to clarify that this contribution does not represent a proper physical uncertainty in the metrological sense, but rather a sensitivity band associated with the fitting procedure. Specifically, it stems from the dispersion of results within the P5-P95 percentile range obtained by varying the fitting parameters within reasonable bounds. The statistical uncertainty was controlled through long acquisition times: velocity signals were recorded for 20 s at a sampling frequency of 100 kHz. This choice represents a trade-off between statistical convergence of turbulence quantities and practical testing duration, ensuring sufficient spectral resolution while maintaining reasonable experimental time requirements.

An important observation stemming from this analysis is that a rigorous re-selection of the fitting interval is not required for every individual test case. Once the fitting bounds are defined according to physically consistent criteria, they can be kept fixed and the iterative procedure can be applied systematically across all operating conditions. Only in cases where the Reynolds number changes substantially, leading to a modification of the spectral structure and a shift of the energy-containing and inertial subranges, may a redefinition of the fitting interval become necessary. Outside of such conditions, the methodology can be applied consistently without further adjustments.

In conclusion, the iterative model-based methodology developed in this thesis enhances the robustness, repeatability, and physical consistency of integral length scale estimation from experimental data. When applied within its range of validity, it represents a valuable tool for turbulence characterization in turbomachinery research and offers a structured framework that can be extended to future experimental campaigns and different flow conditions.

Bibliography

[1] G. K. Batchelor. *The Theory of Homogeneous Turbulence*. Cambridge University Press, Cambridge, 2nd edition, 1971.

[2] A. Bauer. *Automated Hybrid Time Series Forecasting: Design, Benchmarking, and Use Cases*. Dissertation, Julius-Maximilians-Universität Würzburg, Würzburg, Germany, 2020.

[3] F. Bertelli, M. Okada, S. Lavagnoli, and K. Hillewaert. An active turbulence grid for turbomachinery flow experiments. In *Proceedings of the ASME Turbo Expo 2024: Turbomachinery Technical Conference and Exposition*, number GT2024-128565 in GT2024, London, United Kingdom, June 2024. ASME.

[4] E. Boufidi. *The Characterization of Turbulence in High Speed Compressible and Complex Industrial Flows*. Phd thesis, Université Catholique de Louvain, Louvain-la-Neuve, Belgium, October 2020. In collaboration with the von Karman Institute for Fluid Dynamics.

[5] E. Boufidi, S. Lavagnoli, and F. Fontaneto. A probabilistic uncertainty estimation method for turbulence parameters measured by hot-wire anemometry in short-duration wind tunnels. *Journal of Engineering for Gas Turbines and Power*, 142(3): 031007, March 2020. doi: 10.1115/1.4044780.

[6] G. L. Brown and A. Roshko. On density effects and large structure in turbulent mixing layers. *Journal of Fluid Mechanics*, 64(4):775–816, 1974.

[7] H. H. Bruun. *Hot-Wire Anemometry: Principles and Signal Analysis*. Oxford University Press, Oxford, 1995. ISBN 978-0-19-856342-6.

[8] P. Burattini and R. A. Antonia. The effect of different x-wire calibration schemes on some turbulence statistics. *Experiments in Fluids*, 38:80–89, 2005. doi: 10.1007/s00348-004-0889-9.

[9] B. Cukurel and W. K. George. A novel perspective to high-speed cross-hot-wire

calibration methodology. *Experiments in Fluids*, 53(3):713–729, 2012. doi: 10.1007/s00348-012-1313-1.

[10] L. D. de Santana. *Semi-analytical methodologies for airfoil noise prediction.* Phd thesis, KU Leuven, Heverlee, Belgium, September 2015.

[11] J. D. Denton. Some limitations of turbomachinery CFD. In *Proceedings of ASME Turbo Expo 2010: Power for Land, Sea and Air*, GT2010, Glasgow, UK, June 14-18 2010. ASME. Paper No. GT2010-22540.

[12] C. F. J. Dewey. A correlation of convective heat transfer and recovery temperature data for cylinders in compressible flow. *International Journal of Heat and Mass Transfer*, 8:245–252, 1965.

[13] J. O. Hinze. *Turbulence.* McGraw-Hill, New York, 2nd edition, 1975.

[14] F. E. Jørgensen. How to measure turbulence with hot-wire anemometers: A practical guide. Technical report, Dantec Dynamics A/S, Skovlunde, Denmark, 2005.

[15] L. V. King. On the Convection of Heat From Small Cylinders in a Stream of Fluid: Determination of the Convection Constants of Small Platinum Wires With Applications to Hot-Wire Anemometry. *Philosophical Transactions of the Royal Society of London. Series A*, 214(509–522):373–432, 1914. doi: 10.1098/rsta.1914.0023.

[16] A. N. Kolmogorov. The local structure of turbulence in incompressible viscous fluid for very large Reynolds numbers. *Dokl. Akad. Nauk SSSR*, 30:299–303, 1941.

[17] P. K. Kundu, I. M. Cohen, and D. R. Dowling. *Fluid Mechanics.* Academic Press, Waltham, MA, 5th edition, 2012. ISBN 978-0-12-382100-3.

[18] J. Lewalle and D. E. Ashpis. Estimation of time scales in unsteady flows in a turbomachinery rig. Technical Memorandum NASA/TM-2004-209452, National Aeronautics and Space Administration, Glenn Research Center, Cleveland, Ohio, February 2004. URL `http://gltrs.grc.nasa.gov`.

[19] G. Lopes, L. Simonassi, S. Gendebien, A. F. M. Torre, M. Patinios, N. Zeller, L. Pintat, and S. Lavagnoli. An open test case for high-speed low-pressure turbines: The spleen c1 cascade. *International Journal of Turbomachinery, Propulsion and Power*, 10(1), 2025.

[20] R. E. Mayle. The role of laminar-turbulent transition in gas turbine engines. *Journal of Turbomachinery*, 113(4):509–537, 1991. doi: 10.1115/1.2927904.

[21] W. D. McComb. *Homogeneous, Isotropic Turbulence: Phenomenology, Renormaliza-*

tion and Statistical Closures. Number 162 in International Series of Monographs on Physics. Oxford University Press, first edition, 2014.

[22] D. O. Mora and M. Obligado. Estimating the integral length scale on turbulent flows from the zero crossings of the longitudinal velocity fluctuation. *Experiments in Fluids*, 61(9):1–15, 2020. doi: 10.1007/s00348-020-03035-1.

[23] K. A. Nagabushana and P. C. Stainback. Heat transfer from cylinders in subsonic slip flows. NASA Contractor Report NASA CR-4429, National Aeronautics and Space Administration, Hampton, VA, 1992.

[24] P. L. O'Neill, D. Nicolaides, D. Honnery, and J. Soria. Autocorrelation functions and the determination of integral length with reference to experimental and numerical data. In *Proceedings of the 15th Australasian Fluid Mechanics Conference*, pages 1–4, Sydney, Australia, 2004.

[25] G. Pastorino, E. Boufidi, K. Hillewaert, and F. Fontaneto. Aerodynamic scaling of a high-speed low-pressure turbine cascade, optimized for boundary layer similarity in a low-speed test rig. In *Proceedings of the 16th European Turbomachinery Conference (ETC16)*, Hannover, Germany, March 2025. Paper ID: ETC2025-214.

[26] S. B. Pope. *Turbulent Flows*. Cambridge University Press, Cambridge, UK, 2000.

[27] L. F. Richardson. *Weather Prediction by Numerical Process*. Cambridge University Press, Cambridge, 1922.

[28] P. E. Roach. The generation of nearly isotropic turbulence by means of grids. *International Journal of Heat and Fluid Flow*, 8(2):82–92, 1987. doi: 10.1016/0142-727X(87)90001-4.

[29] N. Rosafio, G. Lopes, S. Salvadori, S. Lavagnoli, and D. A. Misul. Rans prediction of losses and transition onset in a high-speed low-pressure turbine cascade. *Energies*, 16(21):7348, 2023. doi: 10.3390/en16217348.

[30] W. Sutherland. The viscosity of gases and molecular force. *Philosophical Magazine*, 36:507–531, 1893. doi: 10.1080/14786449308620508.

[31] M. Tagawa, T. Tsuji, and Y. Nagano. Evaluation of x-probe response to wire separation for wall turbulence measurements. *Experiments in Fluids*, 12:413–421, 1992.

[32] G. I. Taylor. The spectrum of turbulence. *Proceedings of the Royal Society of London. Series A-Mathematical and Physical Sciences*, 164(919):476–490, 1938.

[33] H. Tennekes and J. L. Lumley. *A First Course in Turbulence*. MIT Press, Cambridge, MA, 1972. ISBN 978-0262200196.

[34] von Karman Institute for Fluid Dynamics. Low speed cascade wind tunnel c-1. `https://www.vki.ac.be/index.php/57-research-and-consulting/facilities/turbomachinery-facilities/86-low-speed-cascade-wind-tunnel-c-1`.

[35] T. von Kármán. Progress in the statistical theory of turbulence. *Proceedings of the National Academy of Sciences of the United States of America*, 34(11):530–539, 1948.

[36] P. D. Welch. The use of fast fourier transform for the estimation of power spectra: A method based on time averaging over short, modified periodograms. *IEEE Transactions on Audio and Electroacoustics*, AU-15(2):70–73, 1967. doi: 10.1109/TAU.1967.1161901.

[37] A. M. Yaglom. *Correlation Theory of Stationary and Related Random Functions*. Springer-Verlag, New York, 1987.

A| Effect of XW probe geometry on isotropy measurements

During the experimental campaign, several important observations were made regarding the influence of probe geometry on turbulence measurements, particularly with respect to yaw sensitivity and anisotropy estimation. In the early stages of testing, a custom cross-wire (XW) probe with a geometric angle of 140° between the wires was adopted. However, after identifying inconsistencies in the turbulence statistics measured, the standard *Dantec* 55P51 probe, featuring perpendicular wires, was subsequently employed for comparison and validation purposes.

As discussed by Burattini and Antonia [8], increasing the geometric angle θ_g reduces the yaw sensitivity of a cross-wire probe. When the included angle between the wires is increased, each wire becomes closer to being perpendicular to the mean flow direction. As a consequence, variations in yaw angle produce smaller differences in the electrical response of the two wires. This behavior is clearly observed in Fig. A.1. Increasing the included angle from 90° (Dantec X-wire) to 140° (custom X-wire) significantly flattens the calibration curve. The custom probe exhibits a much weaker variation of Re_{eff}/Re with yaw angle compared to the *Dantec* probe. Therefore, for a given angular fluctuation, the large-angle configuration generates a smaller change in output, indicating reduced sensitivity to transverse velocity fluctuations.

This reduced yaw sensitivity has direct implications for turbulence statistics, as it decreases the robustness of the velocity decomposition. In particular, Tagawa, Tsuji, and Nagano [31] demonstrated that larger θ_g values tend to overestimate the r.m.s. of the transverse velocity component, while the streamwise r.m.s. remains largely unaffected. This effect is clearly illustrated in Fig. A.2, where the turbulence intensity Tu and isotropy ratio obtained with the two probes are compared for a pitchwise measurement. The value of Tu does not vary significantly between the probes, reflecting the fact that the dominant streamwise component remains essentially unchanged. In contrast, the isotropy ratio

shows a marked decrease for the custom probe, yielding values around $0.7 - 0.8$, whereas the *Dantec* probe measures values around $1.1 - 1.2$, consistent with literature data [28]. Since the streamwise component is generally less affected by wire separation and angular sensitivity errors, the reduction in the isotropy ratio confirms that the transverse component v_{rms} is overestimated by the custom probe.

These findings demonstrate that probe geometric configuration alone can significantly bias conclusions regarding turbulence structure and isotropy.

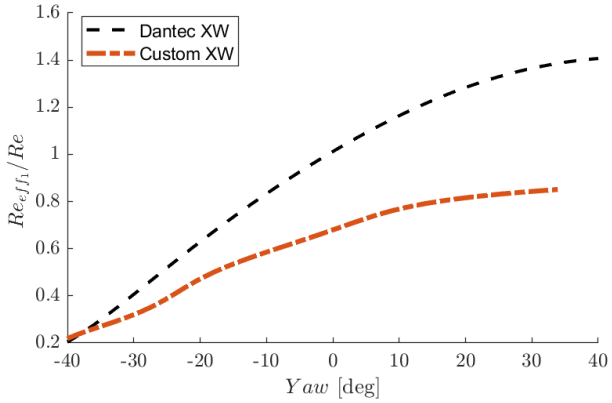

Figure A.1: Angular sensitivity curves for the Dantec and custom cross-wire probes (XW)

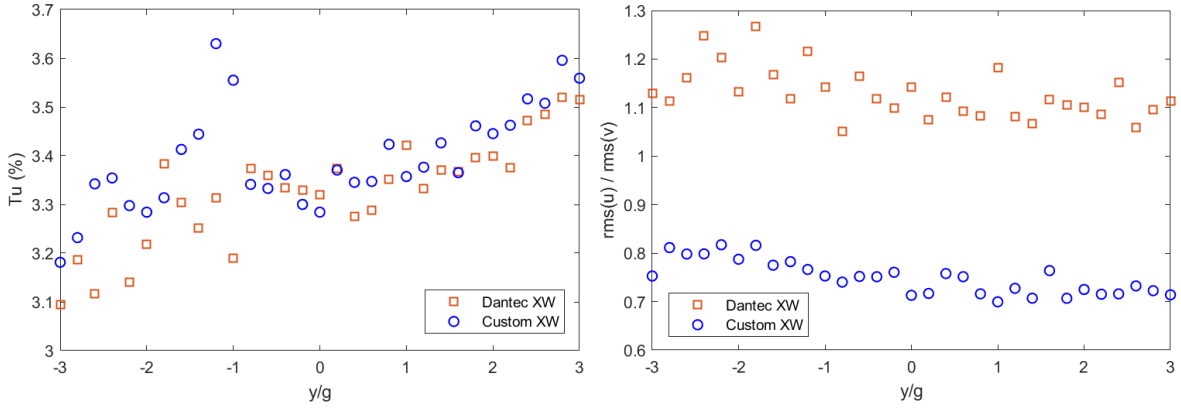

(a) (b)

Figure A.2: Comparison of turbulence statistics obtained with the Dantec and custom cross-wire probes (XW) along the pitchwise direction y/g, where g is the blade pitch. (a) Turbulence intensity Tu. (b) Isotropy ratio $u_{\mathrm{rms}}/v_{\mathrm{rms}}$.

Ringraziamenti

In quest'ultima parte della tesi vorrei in particolar modo ringraziare le persone che mi hanno seguito e offerto il loro tempo e aiuto per rendere possibile questo progetto. Prima di tutto vorrei sottolineare come questi sei mesi passati in Belgio, al von Karman institute, abbiano rappresentato un'occasione di crescita personale e professionale e non solo, anche un'importante rampa di lancio per il lavoro futuro. Per avermi dato questa possibilità voglio ringraziare il professor Paolo Gaetani che in questi mesi ha seguito a distanza il mio lavoro. Vorrei rivolgergli un ringraziamento anche per aver dimostrato cura e interesse nella crescita dei suoi studenti organizzando importanti esperienze educative, in primis il laboratorio di turbomacchine, e mettendo il suo tempo a disposizione. In secondo luogo vorrei ringraziare il professor Fabrizio Fontaneto che ha coordinato il progetto in prima persona al von Karman Institute. I suoi consigli sono stati essenziali per strutturare e indirizzare il mio lavoro spingendomi, inoltre, a una valutazione critica di quanto svolto. Insieme al prof. Fontaneto ringrazio Elissavet Boufidi per la sua competenza, gentilezza e disponibilità. Che questo sia l'inizio di una fantastica collaborazione.
Infine, ultimo ma non per importanza, un grosso ringraziamento è rivolto a Giacomo Pastorino che rappresenta forse la vera colonna portante su cui si regge questa tesi. Abbiamo condiviso dubbi, disperazioni e idee sia sul lavoro, ma anche sul futuro. Non finirò mai di ringraziarlo per avermi dato tanto e tanto del suo tempo e aver dimostrato davvero quanto tiene a cuore il successo e la realizzazione dei suoi studenti. Sarà per sempre un mentore e un amico prezioso.